JGR Space Physics

RESEARCH ARTICLE
10.1029/2022JA031197

Key Points:

- Electron heat flux formation in diffuse aurora associated with electron precipitation events
- Simulated electron thermal fluxes during the St. Patrick's 2013 and 2015 storms
- Thermal electron heat flux validation using Defense Meteorological Satellite Program observations

Correspondence to:

G. V. Khazanov,
George.V.Khazanov@nasa.gov

Citation:

Khazanov, G. V., Chen, M. W., Mishin, E. V., & Chu, M. (2023). Thermal electron heat fluxes associated with precipitated auroral electrons during the Saint Patrick's Days 2013 and 2015 geomagnetic storms. *Journal of Geophysical Research: Space Physics*, *128*, e2022JA031197. https://doi.org/10.1029/2022JA031197

Received 30 NOV 2022
Accepted 30 JAN 2023

Author Contributions:

Conceptualization: George V. Khazanov
Data curation: Margaret W. Chen, Evgeny V. Mishin, Mike Chu
Formal analysis: George V. Khazanov
Investigation: George V. Khazanov
Methodology: George V. Khazanov
Resources: George V. Khazanov
Software: George V. Khazanov
Supervision: George V. Khazanov
Validation: George V. Khazanov
Visualization: George V. Khazanov, Mike Chu
Writing – original draft: George V. Khazanov
Writing – review & editing: George V. Khazanov, Margaret W. Chen, Evgeny V. Mishin

Thermal Electron Heat Fluxes Associated With Precipitated Auroral Electrons During the Saint Patrick's Days 2013 and 2015 Geomagnetic Storms

George V. Khazanov[1], Margaret W. Chen[2], Evgeny V. Mishin[3], and Mike Chu[4]

[1]NASA Goddard Space Flight Center, Greenbelt, MD, USA, [2]The Aerospace Corporation, El Segundo, CA, USA, [3]Air Force Research Laboratory, Albuquerque, NM, USA, [4]The Space Weather Lab, George Mason University, Fairfax, VA, USA

Abstract The Rice Convection Model-Equilibrium (RCM-E) and SuperThermal Electron Transport (STET) are combined to investigate electron heat flux formation in the region of the diffuse aurora for the geomagnetic storms of 17 March 2013 and 17 March 2015. The primary electron precipitation into the atmosphere resulting from wave particle scattering in the magnetosphere are simulated by the magnetically and electrically RCM-E during these two geomagnetic storms. The primary precipitating electron fluxes are modified by the STET model by taking into account atmospheric backscatter processes. The modified electron energy fluxes and their mean energies are coupled to the STET code to calculate electron thermal fluxes associated with diffuse aurora on a global scale. We use the simulated heat flux to estimate electron temperatures at the upper ionospheric altitudes and compare them with corresponding observations from the Defense Meteorological Satellite Program satellite.

1. Introduction

Electron thermal heat fluxes continue to be one of the puzzling phenomena that create some difficulties for the ionospheric modeling networks in the calculation of electron temperature (Bekerat et al., 2007; Glocer et al., 2017, 2012; Richmond et al., 1992; Ridley et al., 2006; Schunk et al., 1986). This is especially true in the high latitude ionosphere, specifically in the aurora, which is connected via the closed geomagnetic field lines with the large energy reservoir, Earth's plasma sheet.

The electron heat flux in the ionosphere is carried by electrons with energies below 1 eV but this parameter is not directly measurable by any existing experimental space plasma techniques. The electron heat flux is usually specified by comparing simulated electron temperatures with available observations. A classic example of such an approach was presented by Schunk et al. (1986) in their theoretical study of the electron temperature T_e in the high-latitude ionosphere for solar maximum and winter conditions. As pointed out in their analysis, "the high-latitude ionosphere interfaces with the hot, tenuous, magnetospheric plasma, and a heat flow into the ionosphere is expected". The approach that Schunk et al. (1986) developed was very useful for identifying the role of the electron heat fluxes in the explanation of radar measurement measurements of very high T_e at Sondrestrom (Kofman & Wickwar, 1984), and DE 2 satellite measurements (Curtis et al., 1985; Fontheim et al., 1987) where electron temperatures were in the range of about 5000–10000 K.

Based on the processes that are involved in the formation of magnetospheric heat fluxes, they can be classified as locally or non-locally formed. The *locally formed* magnetospheric heat fluxes result from the direct interaction of the hot particles or waves of magnetospheric origin with the cold background magnetospheric electrons. Cole (1965) introduced heating of the thermal electron by ring current (RC) protons and Kozyra et al. (1987) included the RC atomic oxygen as the most effective source in the production of electron heat fluxes. The hot electron component of the Earth's plasma sheet also contributes to the heat flux formation and its efficiency depends on the magnetospheric conditions (Khazanov, 2010).

Cornwall et al. (1971) suggested that Landau damping of electromagnetic ion cyclotron (EMIC) waves on the magnetospheric thermal electrons can also be the source of these thermal fluxes. Hasegawa and Mima (1978) discussed the damping of kinetic Alfven waves as the contributor to the magnetospheric electron heating. Sometimes the magnetospheric hot plasma population and waves are interconnected and both participate in the heating of the thermal electrons. Khazanov et al. (2007) considered both RC Coulomb collisions and EMIC waves

contribution to the formation of the thermal electron heat fluxes that are self-consistently calculated for the specific magnetospheric storm conditions. In addition, nonlinear coupling with lower hybrid waves was shown to be an effective source of heating of thermal electrons in the RC region (Mishin, 2013; Mishin & Burke, 2005).

The thermal background magnetospheric electron population can also be locally heated by the sources of non-magnetospheric origin and create *non-locally formed* electron thermal fluxes. Such processes are affiliated with photo- and secondary electrons (SEs) production at ionospheric altitudes. Photoelectrons are produced by the interaction of solar ultraviolet (UV) and X-Ray radiation with the neutral atmosphere and the secondary ones are produced via corresponding collisions of high-energy precipitated particles of magnetospheric origin (Khazanov, 2010; Schunk & Nagy, 2009). These superthermal electron populations with energies below about 500 eV can escape from the ionospheric altitudes and be trapped in the magnetosphere via the Coulomb collisions with thermal electrons and ions and wave-particle interaction processes (Khazanov et al., 2020). The interaction of these populations with the thermal electrons forms the downward electron heat flux to ionospheric altitudes and along with locally formed magnetospheric fluxes (as mentioned above) form the upper boundary electron temperature conditions for global ionospheric modeling networks.

Identification of the above-mentioned processes in the formation of electron thermal heat fluxes was an important step for establishing the electron heat flux calculation especially during magnetospheric storms and substorms. Recent studies by Khazanov et al. (2020, 2022), Khazanov, Glocer, and Chu (2021), and Khazanov, Sibeck, et al. (2019) used the SuperThermal Electron Transport (STET) model to compute steady-state electron heat flux in different ionospheric regions for prescribed electron distributions in the diffuse aurora. These results were partially applied to calculate electron thermal fluxes during one of the substorms at 09:40:00 UT across Canada and Alaska (Khazanov et al., 2022).

This paper investigates the heat flux formation associated with diffuse auroral precipitating electrons in the high latitude ionosphere on a global scale during the St. Patrick's Days 2013 and 2015 geomagnetic storms. To do this we couple the magnetically and electrically self-consistent Rice Convection Model-Equilibrium (RCM-E; Chen et al., 2012, 2019; Lemon et al., 2004) with STET as described by Khazanov, Chen, et al. (2019), and further discussed by Khazanov and Chen (2021) in the application to the region of diffuse aurora. The precipitating auroral electrons with energies above ~100 eV that are initially driven by wave-particle interactions (WPIs) in the magnetosphere in the RCM-E are referred in this paper as "precipitating electron fluxes". The fluxes associated with the thermal population of electrons that are calculated in STET are referred to as "heat/thermal electron fluxes". The *novelty* of this paper is the *global simulation* of the storm time thermal heat flux associated with the diffuse auroral electron precipitation that can account for observed increases in ionospheric electron temperature at high latitudes and its affiliated applications.

This paper is organized into the following sections. Section 2 presents the general characteristics of the St. Patrick's Days 2013 and 2015 geomagnetic storms. Section 3 provides electron thermal flux formation based on the coupling of two kinetic codes: RCM-E and STET. Simulation results of RCM-E/STET code-based electron precipitated and heat fluxes for the two storm events are presented in Section 4. To validate the methodology of the RCM-E/STET heat flux calculations, Sections 5 and 6 present comparisons of simulated results with Defense Meteorological Satellite Program (DMSP) electron temperature observations during St. Patrick's Days of 2013 and 2015 geomagnetic storms. Finally, Section 7 summarizes the major results of this manuscript.

2. St. Patrick's 2013 and 2015 Geomagnetic Storms

Magnetic storms and substorms result from a complex interaction of the solar wind (SW) with the Earth's magnetosphere and ionosphere. They reconfigure the near-Earth geospace environment and cause major increases in energetic particles in the auroral zone, making them an impactful component of space weather. The disturbed magnetosphere and ionosphere (MI) affect the atmosphere and magnetosphere-ionosphere-atmosphere (MIA) coupling processes that are the major focus of our studies in this manuscript.

We simulate the MIA coupling processes associated with diffuse auroral precipitation for two large coronal mass ejection (CME) driven magnetic storms that occurred on 17 March 2013 (Saint Patrick's 2013) and on 17 March 2015 (Saint Patrick's 2015). These storms commence on the same day of year during equinox and thus have similar solar illumination and ionospheric conditions. However, the level of enhanced SW dynamic pressure during southward interplanetary magnetic field (IMF) that drives magnetospheric convection differ for the two storms. Figure 1 shows time traces of SYM-H, SW dynamic pressure, and the IMF components for the Saint Patrick's

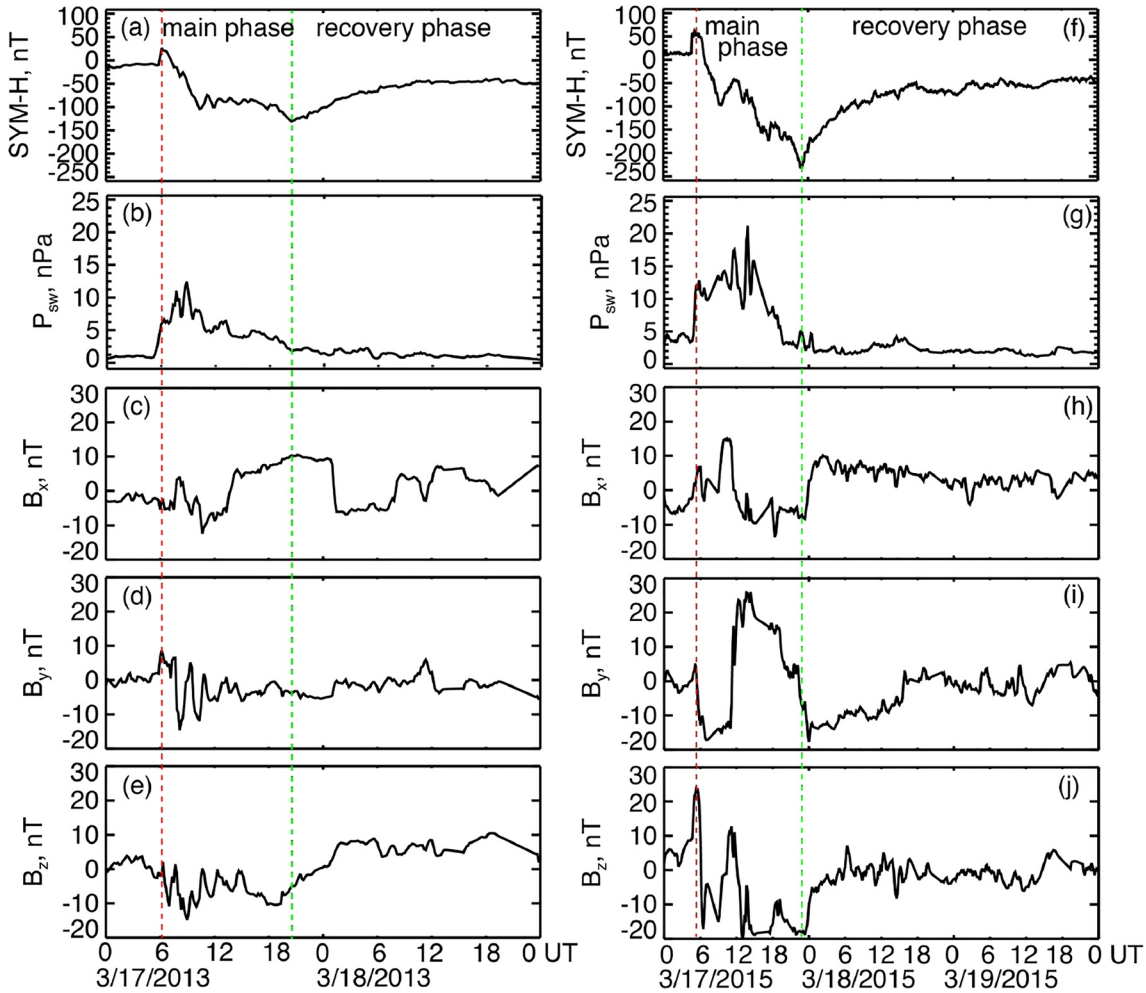

Figure 1. The solar wind (SW) conditions and geomagnetic activity indices for the 2013 and 2015 St. Patrick geomagnetic storms. Time traces of (a, f) SYM-H, (b, g) the SW dynamic pressure P_{sw}, (c, h) the IMF B_x, (d, i) B_y, and (e, j) B_z for the Saint Patrick's 2013 and Saint Patrick's 2015 storm.

2013 (left column) and the Saint Patrick's 2015 (right column) storm. These data were downloaded from the NASA OMNIWeb: omniweb.gsfc.nasa/gov/ow_min.html. The Saint Patrick's Day 2013 storm was caused by a CME that was observed by NASA's Advanced Composition Explorer (ACE) on 17 March 2013 at 06:28 UT. After the sudden commencement at 07:20 UT on 17 March 2013, SYM-H (Figure 1a), a one-minute resolved measurement of *Dst*, becomes negative and the storm main phase begins. During the storm main phase, the IMF B_z (Figure 1e) is southward and the SW dynamic pressure P_{sw} (Figure 1b) is enhanced with a maximum value of 12.4 nPa. The minimum SYM-H is −132 nT at 21:00 UT after which the storm slowly recovers. During this event, the auroral oval is observed from ground-based and in situ observations to expand equatorward to mid-latitudes primarily during the convection phase (Lyons et al., 2016).

The Saint Patrick's Day 2015 storm was driven by a CME that occurred on 17 March 2015 at 02:00 UT. The main phase of the storm started at 06:55 UT and developed in two steps (see Figure 1f). During the first step, a decrease in SYM-H of 100 nT was driven by the southward IMF in the sheath region (Kataoka et al., 2015). The southward IMF in the magnetic cloud pushed the second step of the main phase. During the second step, SYM-H reached a minimum value of −233 nT and the maximum SW dynamic pressure was 21.2 nPa. This was followed by a recovery phase of roughly 2 days. Based on several citizen observations reported by Case and MacDonald (2015), the visible aurora for the Saint Patrick's 2015 storm occurred at low latitudes.

Analyzing the electron heat thermal flux formation below during these two geomagnetic storms, we will be focusing on MIA energy interplay that was only *initially* driven by external SW conditions. As we demonstrate below, such an energy interplay and its further development dramatically depends on ionospheric conditions.

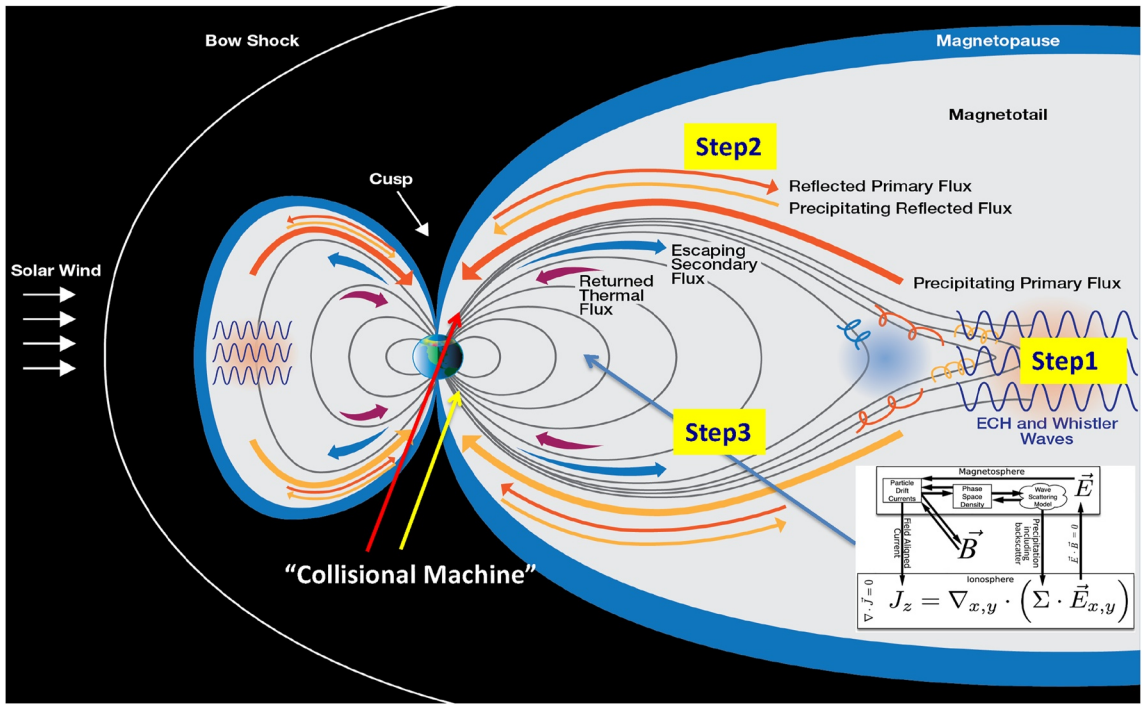

Figure 2. Magnetosphere-ionosphere-atmosphere energy interplay in RCM-E/STET model that produces electron heat fluxes (adapted from Khazanov & Chen, 2021).

3. Thermal Electron Heat Flux Formation: Coupling of RCM-E and STET

Thermal electron heat flux calculations will be based on two well-known and well-documented kinetic codes: RCM-E and STET. These codes are coupled together as described by Khazanov, Chen, et al. (2019) and adjusted in this study for the calculation of thermal electron heat fluxes. This section only outlines the framework that is used in this manuscript to calculate these heat fluxes on the global scale of diffuse aurora occurrence. The heart of the electron heat flux calculation is the STET code that was used in the past for the calculation of this parameter in the regions of midlatitudes (Khazanov, 2010), polar cap (Khazanov, Sibeck, et al., 2019), as well as diffuse (Khazanov et al., 2020; Khazanov, Ma, & Chu, 2022), and discrete auroras (Khazanov, Glocer, & Chu, 2021). We refer readers to these papers for details of such calculations in conjunction with STET code.

RCM-E code is an important element in this study that triggers high energy electron precipitation on the global scale and coupling with STET provides corresponding calculation of electron heat fluxes in RCM-E code simulation domain. Both codes will be briefly outlined below to provide readers with the most important key references of these codes and the guidance of their usage together.

3.1. RCM-E and STET Models Coupling Scenario: Qualitative Picture

The qualitative picture of heat flux formation in aurora was discussed in the papers by Khazanov and Chen (2021), Khazanov et al. (2020), and Khazanov, Ma, and Chu (2022) and is presented here in Figure 2. This figure has been slightly modified from the previous versions to represent the studies that were performed in this paper. The scenario presented here corresponds to the region of diffuse aurora where different kind of WPI processes in the magnetosphere cause the initial precipitation of high energy electron fluxes into the atmosphere. These fluxes, denoted as the *Precipitating Primary Fluxes* (large red and yellow arrows in Figure 2), have pure magnetospheric origin, and deliver their energy to both northern and southern magnetically conjugate regions. In the model presented below, the electron precipitation into the atmosphere is provided by RCM-E code that is briefly described in Section 3.2. This initial process of the formation of precipitated primary fluxes is considered to be the *first step* (Khazanov & Chen, 2021) in the formation of high-energy electron fluxes entering ionospheric altitudes.

The primary precipitating electrons, driven by the RCM-E code at the altitude of 850 km in this study, enter the "collisional machine" (see yellow and red arrows). Some of the primary electrons that precipitate into the

atmosphere are backscattered into the magnetosphere and are denoted as the *Primary Reflected Flux* in Figure 2. Impact ionization and collisions with neutrals cause the energy degradation of the primary electrons and the production of SEs. The mixed population of primary and SEs cascade toward lower energies and some of the SEs escape to the magnetosphere and are denoted as *Escaping Secondary Flux* (blue arrows in Figure 2). There can be multiple backscatters between magnetically conjugate hemispheres. The complex MIA energy interplay are treated by the STET code that is briefly described in Section 3.3 of this manuscript. The modified STET code electron energy fluxes and their mean energies couple back to the RCM-E code to provide the system the MIA feedback to the initial primary precipitation that are driving WPI processes in the RCM-E code. These processes of the formation of precipitated fluxes are considered conceptually to be as the *second step* (Khazanov & Chen, 2021) and represent MIA coupling addition in the formation of high-energy electron fluxes entering ionospheric altitudes.

Modified electron precipitated fluxes by the MIA energy interplay are used in the RCM-E code to update the electric and magnetic fields and the electrodynamic coupling processes on the global scale that in accordance to the terminology by Khazanov and Chen (2021) represent the *third step* in the formation electron energy fluxes. All these three steps that are discussed above are shown in Figure 2. The bock-diagram in Figure 2 will be further elaborated in Section 3.2. Eventually, after these three steps of high energy electron formation, these converged electron precipitated fluxes are passed to the STET code further modifying electron primary reflected flux and escaping secondary flux that are entering back to magnetospheric altitudes providing energy deposition to the background thermal electron and the formation of the *Returned Thermal Flux* that is shown in Figure 2 by purple arrow. The simulation of this thermal/heat flux during St. Patrick's geomagnetic storms is the major focus in this manuscript.

3.2. Rice Convection Model-Equilibrium

The RCM-E combines the Rice Convection Model (RCM; Toffoletto et al., 2003; Wolf, 1983) with a force-Equilibrium magnetic field solver (Lemon et al., 2003) to achieve magnetic self-consistency. The bounce-averaged guiding-center drift motion of isotropic ions and electrons in the closed field line region of the magnetosphere are computed in the RCM. Field-aligned or Birkeland currents that result from the diverging particle drift currents and the electric fields that self-consistently satisfy Ohm's law given an ionospheric conductivity model are calculated.

In Aerospace's version of the RCM-E (see Chen et al., 2015, 2019 for details), there are features that differ from Rice University's RCM-E version (Lemon et al., 2004; Yang et al., 2011, 2015) and we summarize those that are relevant to this study. The magnetic field solver in the RCM-E is more robust and it includes modeling magnetospheric compressions and expansions that improves agreement of simulated magnetic intensity with event data (Chen et al., 2012). The initial inner magnetospheric electron distribution is based on the empirical AE9 model (Ginet et al., 2013) and a treatment of relativistic electron energy is included. Our version calculates the mean precipitating integrated electron energy flux from simulated phase space distributions (see Chen et al., 2015), rather than from an assumption of a Maxwellian electron distribution in the Rice version of the RCM-E. There is an option to include modifications to the integrated electron energy flux and mean electron energy that include the effects of atmospheric backscatter as calculated from the STET model (Khazanov, Chen, et al., 2019). The modified integrated electron energy flux and mean electron energy are used for the conductance calculation that is described below.

The electron loss model includes the effect of scattering due to statistical observations of waves properties with magnetic activity. Orlova and Shprits (2014) (OS) computed pitch-angle diffusion coefficients $D_{w\alpha\alpha}$ against whistler chorus for electrons with energies E between 1 keV and 2 MeV over equatorial geocentric distances normalized by Earth radii R_0 from 3 to 8 for different Kp values and four magnetic local time (MLT) sectors from 21 MLT eastward to 15 MLT. The quantity $1/D_{w\alpha\alpha}$ as functions of Kp, E, R_0, and MLT are provided in OS. Since diffusion coefficients for chorus waves are relatively monotonic, Chen et al. (2019) set the scattering rate against whistler chorus to be $\lambda_w = D_{w\alpha\alpha}$ and use this outside the plasmasphere following (Shprits et al., 2006). Orlova et al. (2014) (OSS) performed a Kp and MLT-parameterization of the reciprocal of the pitch angle diffusion coefficients $D_{h\alpha\alpha}$ against plasmaspheric hiss waves for electron energies between 1 keV and 10 MeV and for R_0 from 3 to 6. The scattering rate against plasmaspheric hiss is taken to be $\lambda_h = D_{h\alpha\alpha}$ and we apply that inside the plasmasphere. In the plasmapause region, they use a logarithmically weighted (by density) average of the lifetime against whistler chorus and hiss (see Chen et al., 2019, 2015 for details). For the purpose of determining which loss rate to use,

the location of the plasmapause is determined from the simulated cold or zero kinetic energy electron density n_e. The definition for inside the plasmapause if $n_e > 100$ cm^{-3}, outside the plasmapause is $n_e < 10$ cm^{-3}, and in the plasmapause region is $10 < n_e < 100$ cm^{-3}.

Proton and oxygen ion losses due to charge exchange with neutral H in the atmosphere are calculated. Ion precipitation due to field-line curvature (FLC) scattering (Sergeev et al., 1983) is included. The ion lifetime against FLC is given by $\tau_{ion\_FLC} = \text{minimum}\,(100 \cdot \varepsilon^5, 1) \cdot \tau_{ion\_strong}$, where ε is the ratio of the gyroradius to the radius of curvature and τ_{ion_strong} is the ion strong diffusion lifetime.

The Pedersen and Hall ionospheric conductance model includes contributions from the solar extreme ultraviolet (EUV) and ionization by precipitating auroral electrons and ions. We use the empirical IRI-2007 (Bilitza & Reinisch, 2008) model to specify the EUV contribution that is kept constant during the simulation. The conductance contribution associated with the diffuse auroral precipitating particles is calculated from the magnetospheric particle distribution at every 5 min of simulation time although the RCM-E results are output at every 10 min. For protons, the auroral Pedersen and Hall conductances are calculated using the Galand and Richmond (2001) formulas that depend on proton energy flux and mean energy. For electrons, there is an option to use the Robinson et al. (1987) formulas that depend on the electron energy flux and mean energy. An alternative method is to use conductances from look up tables of computations from the Boltzmann Three Constituent (B3C) auroral transport model of Strickland et al. (1976, 1993). The B3C code calculates the electron, proton, and H atom fluxes from a coupled set of linear Boltzmann equations with full collisional processes (Basu et al., 1992) over the altitudes of 90–500 km using the empirical NRLMSISE-00 model (Picone et al., 2002). For the look up table, an incident Maxwellian electron spectrum at 500 km is used with the integrated energy flux and mean energy as input parameters.

The primary inputs to the RCM-E are the outer boundary conditions (BCs): the magnetic field, electric potential, and the plasma distribution for each species. This boundary maps to R_b in the equatorial plane except where it is limited by the magnetopause. We set R_b to be at 10 R_E and the quiet time high magnetic latitude boundary was 67°. Chen et al. (2019) describe in detail the time-dependent BCs based on available in situ observations are specified for the St. Patrick's Day 2013 storm. For the St. Patrick's Day 2015 storm, the electric field BCs are based on the Weimer (2001) model that depends on upstream conditions that are provided by the NASA OMNIWeb: omniweb.gsfc.nasa/gov/ow_min.html. The plasma density and temperature BCs are specified using the empirical Tsyganenko and Mukai (2003) model with a modification of a scaling factor of 2 for the plasma sheet temperature because the Tsyganenko and Mukai (2003) model used only low-energy (250 eV–10 keV) particle (LEP) from Geotail spacecraft.

3.3. STET Code

The STET model has a long history. The STET code started with a kinetic treatment of ionospheric photoelectrons by Khazanov (1979) that later was generalized to be used to study many different space plasma phenomena that were well-documented in the book by Khazanov (2010). The most recent usage of STET code was to study auroral space plasma phenomena with the major focus on MIA energy interplay that was driven by different WPI and electrostatic acceleration processes in the region of diffuse (Khazanov et al., 2020) and discrete (Khazanov, Glocer, & Chu, 2021) auroras.

This paper focuses on the formation of electron heat fluxes in the region of diffuse aurora where field-aligned electric field is absent (e.g., Fontaine & Blanc, 1983; Johnstone et al., 1993; Meng et al., 1979; Schumaker et al., 1989) and precipitated electrons are mostly driven by WPI processes. Depending on the nature of wave activities and their space location, STET has been applied to simulate electron precipitation that are triggered by electron cyclotron harmonic whistler-mode choruses (Khazanov et al., 2015) waves, time domain structures (Khazanov, Shen, et al., 2021) as well as modeling of electron interaction with strong hiss wave activity (Khazanov, Ma, & Chu, 2022).

The neutral atmospheric model used in the STET code is the MSIS-90 (Hedin, 1991). The plasma density structure in the ionosphere is based on the IRI-2016 model (Bilitza et al., 2017), and is extended into the magnetosphere based on the plasmaspheric electron density calculation at the geomagnetic equator provided by RCM-E code. Cross sections for elastic collisions, state-specific excitation, and ionization were taken from Solomon et al. (1988).

The STET code solves the gyro-average kinetic equation for the SE for energies above 1 eV and its upper energy limit is not restricted because it includes the relativistic effects (Khazanov, 2010). The kinetic equation for the SE that we used in our study can be presented as (Khazanov, Glocer, & Chu, 2021)

$$\frac{1}{v}\frac{\partial \Phi}{\partial t}+\mu\frac{\partial \Phi}{\partial s}-\frac{1-\mu^2}{2}\left(\frac{1}{B}\frac{\partial B}{\partial s}-\frac{F}{E}\right)\frac{\partial \Phi}{\partial \mu}+EF\mu\frac{\partial}{\partial E}\left(\frac{\Phi}{E}\right)=Q+\langle S\rangle, \quad (1)$$

where $\Phi = 2Ef/m^2$ is the SE flux, f is the electron distribution function, v is SE velocity, t is time, s is the distance along the field line, E is the particle energy, and μ is the cosine of the pitch-angle. F is the electric field force, Q is the SE source term from EUV flux, and $\langle S\rangle$, which includes collision integrals, represents interactions with thermal electrons and ions, scattering with neutral particles, and wave-particle interactions. A detailed derivation of these collisional and wave-particle interaction terms is given in Khazanov (2010) and Khazanov et al. (2015) and all of them are explicitly presented in Khazanov et al. (2020) and Khazanov, Glocer, et al. (2021).

The multiple dissipation processes of magnetospheric electrons in the aurora are affiliated with the cascading of high-energy electrons toward smaller energies and the production of secondary, tertiary, and further resultant electrons. Such ionization cascades can be treated with just a single kinetic equation that takes all the collisional processes into account and seamlessly propagate the solution (Equation 1) along the nonhomogeneous geomagnetic field lines in the presence of WPI processes and with participation of two magnetically conjugate regions of Northern and Southern Hemispheres.

As it was discussed by Khazanov and Chen (2021), and briefly demonstrated in Section 3.4, multiple backscatter phenomena is one of the key and unique element of the STET code that dramatically redistribute initial high energy electron precipitation that is coming from the magnetospheric source (*Step* 1 in Figure 2) and makes a very noticeable change in the electron energy fluxes entering ionospheric altitudes (Khazanov, Chen, et al., 2019; Khazanov, Sibeck, & Chu, 2021). The STET model has been validated with DMSP (Khazanov, Glocer, & Chu, 2021; Wing et al., 2019) and FAST (Khazanov et al., 2016) electron spectra measurements as well with optical observation by Samara et al. (2017) and is believed to be reliable in the studies of electron thermal flux formation at ionospheric altitudes (Khazanov et al., 2022).

3.4. RCM-E/STET Coupling Selected Result

Based on the analysis presented by Khazanov and Chen (2021), Section 3.1 outlines the *3 steps* in the formation precipitated to the atmosphere high-energy electrons driven by the RCM-E/STET coupled code and provides the input to the MIA energy interplay that eventually forms electron thermal heat flux that supports electron temperature, T_e, at upper ionospheric altitude, and as a result, defines the total electron density content that is required for different kinds of space weather applications.

The *first step* that is shown in Figure 2 as *Precipitating Primary Fluxes* is driven by processes that are incorporated in RCM-E code (see Section 3.2 for details) and has the pure magnetospheric origin to begin with. STET code picks up this initial precipitation and enhance these fluxes by considering their multiple atmospheric backscatters with participation of Northern and Southern Hemispheres (*Primary Reflected Flux*) and production of the *Escaping Secondary Flux,* that is one of the biggest contributors to the *Returned Thermal Flux* that is shown in Figure 2 by purple arrow and represents the major focus of study in this manuscript. This process is defined as the *second step* and leads to modification of the ionospheric sources that determine integrated conductance that entering RCM-E and initiate *third step* that presented in Figure 2.

The feedback between conductance and electric potential in RCM-E code modifies the magnetospheric plasma transport and further couples into the magnetic field. Changes to the hot electron drift paths will alter the trapped electron fluxes, while changes in the cold plasma evolution will alter the rate at which the trapped electron fluxes are converted into precipitating fluxes via pitch-angle scattering by chorus and hiss waves. To test the impact of the STET modification, Khazanov, Chen, et al. (2019) applied it to the precipitating electron fluxes computed by the RCM-E, which includes these coupled processes. Because this electrodynamical RCM-E/STET MIA coupling element, the *third step* in the formation electron precipitation phenomena, leads to its dramatic changes, as a result, to the electron heat flux formation. Here we briefly, quantitatively, review this process.

As it is shown by Khazanov et al. (2018), integrated ionospheric conductance is sensitive to the energy distribution of precipitated electrons. Analyzing diffuse auroral electron precipitation effects on RCM-E comparisons

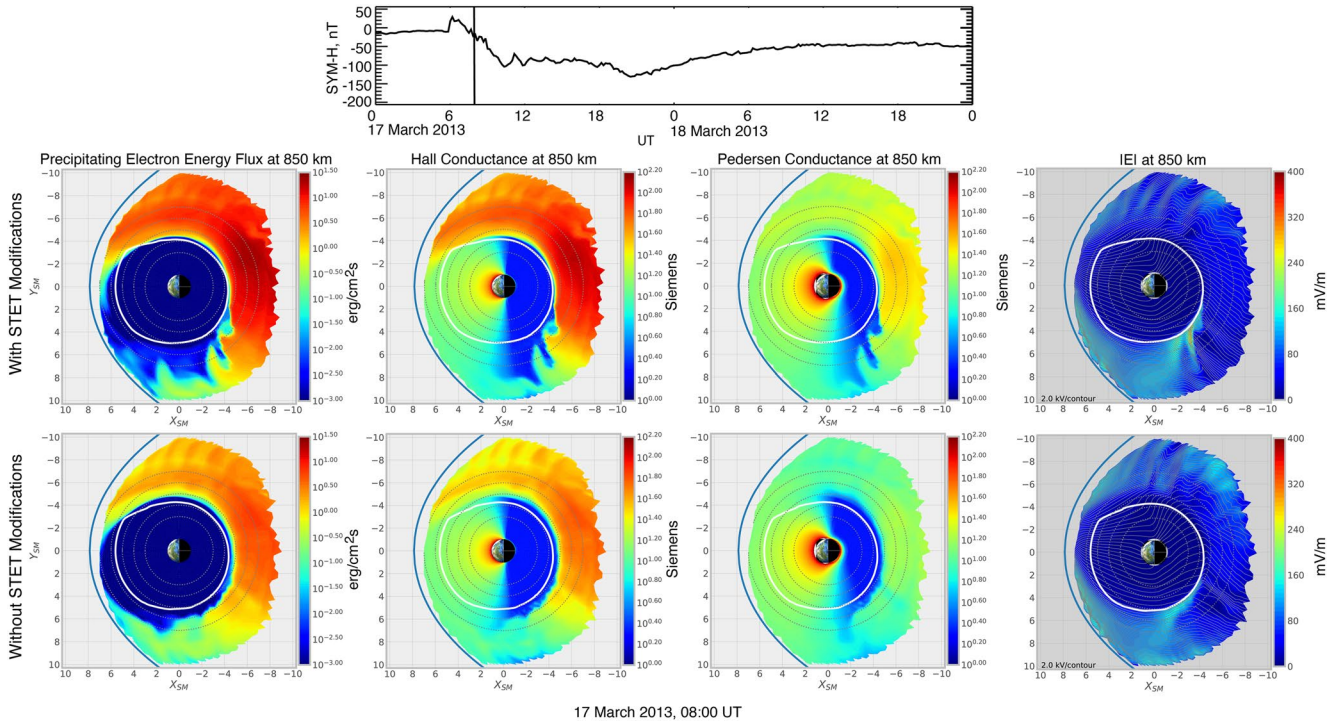

Figure 3. RCM-E/STET coupling selected three steps results.

with satellite data during the 17 March 2013 storm, Chen et al. (2019) presented the simulated electron energy distribution function and found it very close to be to the shape of a Maxwellian one. For that reason, the selected results that are presented below were found for the same geomagnetic storm and used the integrated conductance that assumes Maxwellian distribution function of precipitated high-energy electrons (Khazanov et al., 2018; Robinson et al., 1987).

To understand the global response of MIA SE coupling processes on the results presented below, we emphasize that an increase of the electron energy fluxes at the boundary between the ionosphere and magnetosphere (800–850 km) is the result of the two interconnected magnetically conjugate ionospheric regions and corresponding multiple atmospheric backscatters between them.

Based on our recent studies by Chen et al. (2019), Khazanov and Chen (2021), and Khazanov, Chen, et al. (2019), we briefly summarize MIA coupling elements of RCM-E/STET code with the emphasis on *steps* 2 and 3 of these models.

The results of the analysis presented in the above-mentioned papers revealed that the MIA coupled electron precipitation effects on conductance are quantitatively significant but not always obvious and predictable because of the complex IM electrodynamics (Khazanov, Chen, et al., 2019). Here, in Figure 3, we show examples of the RCM-E simulation results with and without STET modifications at a time early in the main phase of the 17 March 2013 storm. These plots display ionospheric quantities at 850 km mapped to the equatorial plane where the sun is to the left. With STET modifications, there are noticeable differences in the precipitating electron energy flux. These features are seen in the Hall and Pedersen conductance plots. A sharp boundary between high and low conductance on the dusk side forms because a large proportion of the electron population are precipitated before they can reach dusk as their drift speed slows down near kinks in the equatorial equipotential. As seen in Figure 3, there are also large electric intensities associated with very low conductance on the dusk side (see Khazanov & Chen, 2021; Khazanov, Chen, et al., 2019 for additional details). Conversely, where the conductance is high, it is easier to drive currents in the ionosphere and these results in less feedback to the electric field. Thus, there is less shielding of the electric field at lower equatorial distances in the enhanced auroral region with the STET modifications that included backscatter effects than without STET. The reduced shielding allows ions with relatively longer lifetimes than the electrons to be transported to lower L values thereby resulting in enhancing the RC perturbation magnetic field.

4. The Electron Heat Fluxes in Diffuse Aurora

4.1. Electron Heat Flux Kinetic Formalism

The electron heat flux calculation is the final part of the simulation of the coupled RCM-E/STET code after their high-energy electron precipitated fluxes have converged. This part of the calculation is provided only by STET code and these heat flux results are independent from the formation of high-energy precipitated electrons because compared to them, electron heat fluxes carry very small energy fluxes. Typically, in the region of diffuse aurora, electron precipitated energy fluxes are about 1,000 times higher compared to their electron heat flux counterpart (Khazanov et al., 2014, 2017). Nevertheless, as shown below, these small energy fluxes are extremely important in defining the electron temperature of the cold plasma at upper ionospheric altitudes. For this reason, we briefly outline electron heat flux calculation and refer the readers for further details to the following publications (Khazanov, 2010; Khazanov et al., 2020; Khazanov, Glocer, & Chu, 2021).

It should be noted that electron thermal flux calculation presented below (Khazanov et al., 2020; Khazanov, Sibeck, et al., 2019), offers a rigorous and systematic theoretical framework to calculate this value and does not depend on any assumption regarding the form of the core electron distribution function. The electron heat flux entering the upper ionospheric altitude was calculated using STET based methodology presented by Khazanov et al. (2020) and Khazanov, Sibeck, et al. (2019) by integrating the electron-electron and electron-ion collisional term entering SE kinetic Equation 1 over the velocity space:

$$\langle S_{ee}\rangle + \langle S_{ei}\rangle = An_e\left\{\frac{\partial}{\partial E}\left(\frac{\Phi}{E}\right) + \frac{1}{2E^2}\frac{\partial}{\partial \mu}\left[\left(1-\mu^2\right)\frac{\partial \Phi}{\partial \mu}\right]\right\}, \tag{2}$$

where $A = 2\pi e^4 \ln\Lambda$, $\ln\Lambda$ is the Coulomb logarithm, $n_e(s)$ is thermal plasma density, $\Phi = \Phi(s, E, \mu)$ is SE flux. Such an integration of Equation 2 over the energy and pitch-angle variables leads to the expression of SE energy deposition to the thermal electron per unit volume per second as:

$$Q_e(s) = 4\pi A n_e(s)[\Phi_0(E_{\min}) - \Phi_0(E_{\max}) + \int_{E_{\min}}^{E_{\max}} \frac{\Phi_0(E)}{E} dE]. \tag{3}$$

Here Φ_0 is SE omnidirectional flux, and $E_{\min}$ and $E_{\max}$ are taken as 1 eV and 10 keV, correspondingly.

The result of integrating Equation 3 along the field line from the geomagnetic equator, s_{eq}, to the upper ionospheric boundary, s_i, represents the incoming electron heat flux entering the upper ionospheric altitude:

$$q(s_i) = \int_{s_{eq}}^{s_i} Q_e(s)\frac{B_i}{B(s)} ds \tag{4}$$

The STET heat fluxes are mostly contributed by superthermal electron energies below 500–600 eV, and, in the presence of wave activity that drives high energy electron precipitation, are not sensitive to the cold electron density values at geomagnetic equator (Khazanov et al., 2020). In accordance to the classification that is presented in the introduction to this manuscript, these heat fluxes belong to *non-locally formed* electron thermal fluxes.

4.2. St. Patrick's 2013 Magnetic Storm

As it is shown in Figure 1, St. Patrick's 2013 storm started on March 17 at UT = 0 and continued for 2 days. Figure 4 presents the results of coupled RCM-E/STET code simulation during this entire event between 6 and 18 MLT in the simulation domain of MLAT RCM-E code corresponding to the region of diffuse aurora. The windows of first column in this figure corresponds to the precipitated high energy electron fluxes at altitudes of 850 km, the second column shows their mean energies, and the third column is the affiliated thermal electron heat fluxes that is calculated as outlined in Section 4.1. The results presented in Figure 4 and all follow-up coupled RCM-E/STET code simulation data are shown at intervals of 10 min. The results presented in Figure 4 are shown for the two different models of integrated ionospheric conductances, with the widely used Robinson et al. (1987) formulae or conductance that is based on the B3C auroral transport code.

Simulation results for both 2013 and 2015 St. Patrick's 2013 magnetic storm presented in this manuscript only show the data that correspond to precipitated electron energy fluxes above 10^{-3} erg*cm^{-2}*s^{-1} and their mean

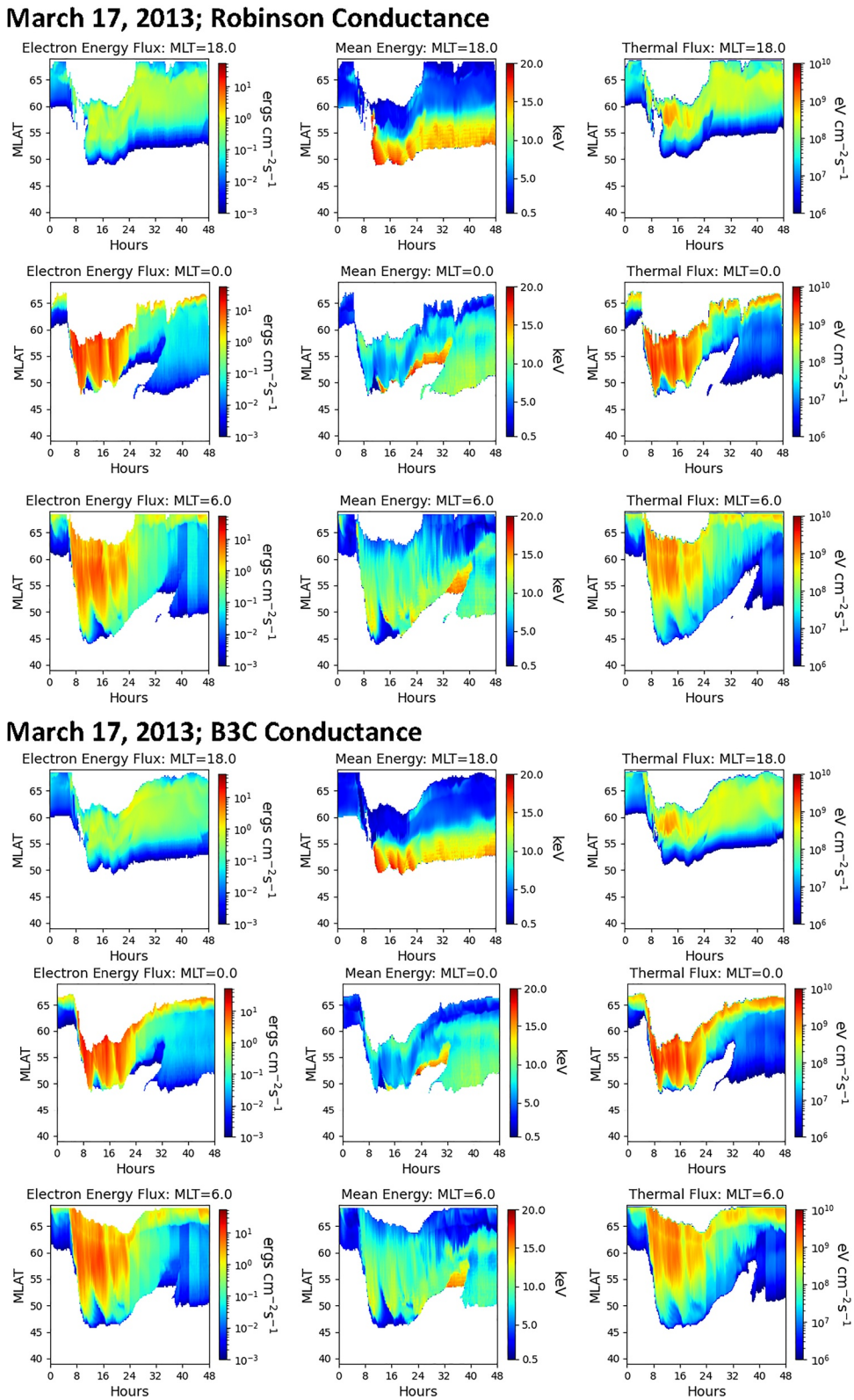

Figure 4. Geomagnetic storm 17 March 2013. RCM-E/STET-driven electron heat fluxes for selected MLTs and different height altitude-integrated conductances.

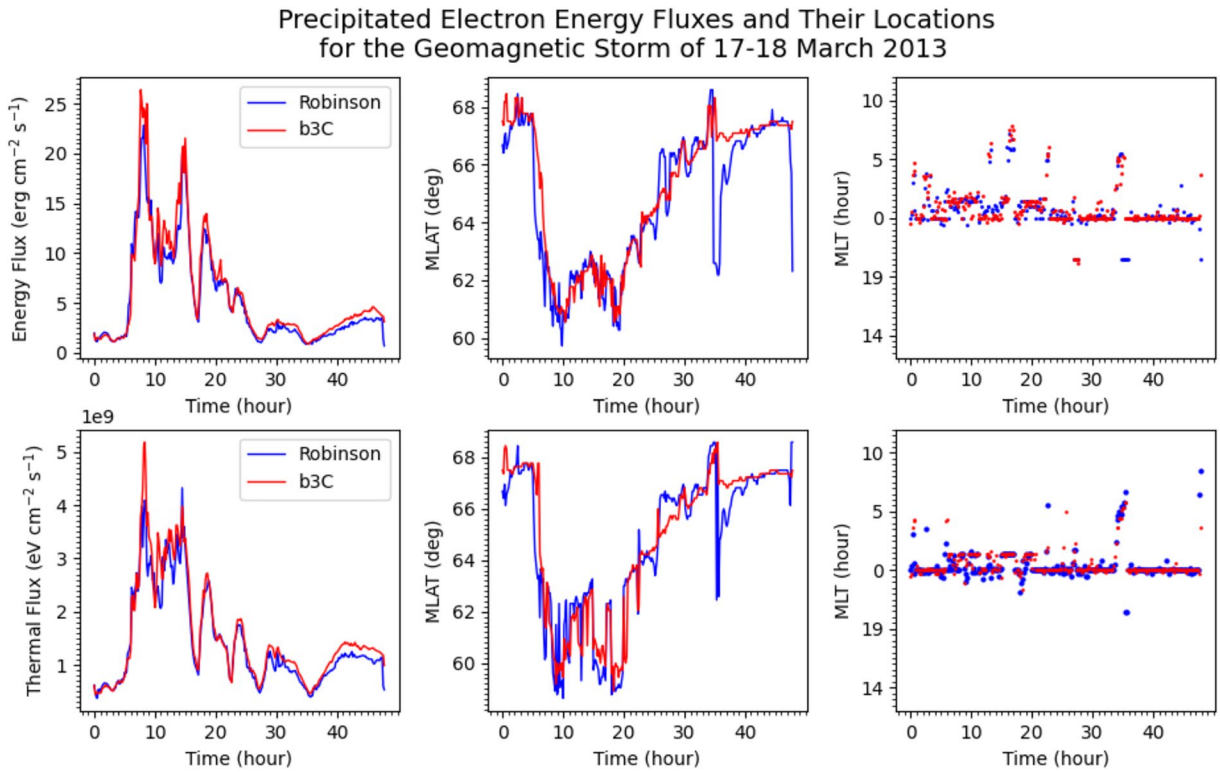

Figure 5. Maximum values of electron precipitation energy and heat fluxes migration over the geomagnetic storm of 17–18 March 2013.

energies above 200 eVs. Correspondingly, affiliated with electron precipitation electron thermal heat fluxes are presented when they exceed the magnitude of 10^6 eV*cm^{-2}*s^{-1}.

At first glance, the results that are presented in Figure 4 appear weakly dependent on the conductance model; however, all values that are presented here are very dynamical during entire storm and require their further analysis and validation. The heat flux in the auroral oval strongly depends on the time history of electron precipitation, and thus it is crucial to obtain physics-based electron precipitation that provides RCM-E code. Statistical models of precipitation (Fuller-Rowell & Evans, 1987; Hardy et al., 1993) that are used in some of the global ionospheric modeling networks would substantially underestimate the precipitation's time variation scales of thermal electron heat fluxes that we consider in this manuscript.

Figure 4 shows only the nighttime of precipitated high-energy electron fluxes, their mean energies, and the corresponding to them electron thermal fluxes. During the main phase of this storm, there are very noticeable, with several orders of magnitude changes, in precipitated electron energy fluxes as they move eastward from the evening, MLT of 18, to the morning sides, MLT of 6. During this time of the storm, both precipitated electron energy fluxes and electron heat fluxes are strongly correlated with each other and are maximized at the midnight at MLT = 0.

Dependence of electron heat fluxes on the mean energy of precipitated electrons driven by RCM-E code is quite different and clearly demonstrated in the third windows of Figure 4. For example, as it is seen from this plot, especially during the recovery phase of St. Patrick's geomagnetic storm 2013 electron, electron heat fluxes increase with decreasing mean energy. As it was previously discussed by Khazanov et al. (2014), this is consistent with the corresponding decrease in the secondary fluxes (blue arrows in Figure 2; "Escaping Secondary Flux") that mostly contribute to the formation of the heat flux that shown in the third window of Figure 4. There are two reasons for this decrease: (a) the decrease in the efficiency of SE production for higher mean energy of precipitated electrons; (b) the higher energy precipitation penetrates further into the atmosphere, and it is therefore more difficult for the generated SEs to escape to contribute to the upward flux.

The location and migration of maximum electron heat values in the region of diffuse aurora, as St. Patrick's geomagnetic storm 2013 develops, are illustrated by Figure 5 together with corresponding precipitation electron

energy fluxes. These two parameters are well correlated with each other and their MLAT and MLT locations are practically the same. Blue and red lines and dots in windows of Figure 5 represent the different models of integrated ionospheric conductance that have been used in simulated scenario of RCM-E/STET codes. Interestingly, that for these two different conductances, the intensity of precipitated electron energy fluxes and corresponding heat fluxes remained to be close to each other during almost the entire storm. Even their positions in RCM-E simulation domain of MLAT and MLT are relatively close to each except during the recovery phase of this storm on 18 March, around UT = 10.72. Apparently such a large MLAT and MLT differences in the location of maximum of these two energy fluxes is related to electric field calculation and will be subject of our further studies in upcoming publications.

In the vicinity of the main phase of the storm precipitated electron energy fluxes and thermal electron heat flux reach their maximum values, move about 8° toward the south in MLAT and mostly locate around MLT = 0–2. As storm progresses the maximum values of these parameters move in the north-east direction reaching dayside of MLTs.

4.3. St. Patrick's 2015 Magnetic Storm

This magnetic storm was much stronger (see Figure 1f) and RCM-E/STET simulations presented in Figure 6 below cover 72 hr of its development. St. Patrick's Day geomagnetic storm 2015 was one of the major space weather events of the 24th solar cycle, and therefore, the simulation of electron heat fluxes as well as affiliated high energy electron fluxes parameters will be presented in more detail emphasizing the importance of these values in the space weather studies.

Figure 6, like Figure 4, as has been shown for the St. Patrick's Day geomagnetic storm 2013 in the previous subsection, demonstrates the development of the thermal electron heat fluxes on the global scale in the conjunction with high energy electron precipitation simulated by RCM-E/STET code. This figure was extended to the dayside of the simulation domain and presents more MLT details as this geomagnetic storm develops. As in the case of the St. Patrick's Day 2013 magnetic storm, there is no visible dependence of the calculated parameters on the integrated ionospheric conductance. This effect will be investigated further and discuss in our forthcoming publications.

Compared to the precipitated electron energy fluxes and corresponding electron thermal heat fluxes, presented in Figure 4 for the 17 March 2013 storm, this, 2015 geomagnetic storm is more powerful and the corresponding values of these parameters are much higher. As can be seen from Figure 6, the functional dependence of electron heat fluxes on the high-energy electron precipitation energy flux and their mean energy during this storm remain to be the same as we discussed in the previous subsection. St. Patrick 2015 simulated parameters penetrate much deeper to the south showing strong and very complicated dynamics down the MLATs around about 40°. Because we are focusing in this manuscript on electron heat fluxes, Figure 7 presents clockwise heat flux MLT dynamics that is viewed from the northern pole.

The thermal heat flux clock of St. Patrick's Day 2015 magnetic field, as it is shown in Figure 7, demonstrates the complex dynamics of thermal electron flux formation of the global scale during disturbed space plasma conditions. As we mentioned above, this parameter, electron thermal flux, is not measurable by any in situ instrumentation, but is required as the BC for the electron temperature calculations. The best one can do is to use an implicit calculation of electron heat fluxes using experimental electron temperature profiles measured by incoherent radar facilities or by rocket flights and connect them via thermal electron conductivity coefficient of the well-known expression for the electron heat flux presented by Banks (1966). Such an approach has been used in the paper by Fallen and Watkins (2013) where they presented long time range electron thermal flux estimation from Poker Flat Incoherent Scatter Radar measurements of electron density and temperature. As these authors pointed out, "ISR-measured profiles above the F2 peak layer are typically noisy and vary with time, making it difficult to estimate the electron temperature gradient in without averaging". These authors used a monthly averaged window that typically does not represent typical noisy electron temperatures seen in a short, storm time conditions development events, which we considered in this manuscript.

Besides, the experimental information of the electron heat fluxes never would be available on the global scale and the approaches that handle the electron heat BCs at the upper ionospheric altitudes in all ionospheric networks, remain to be illusional. That is why the theoretical determination of electron heat fluxes from a similar but

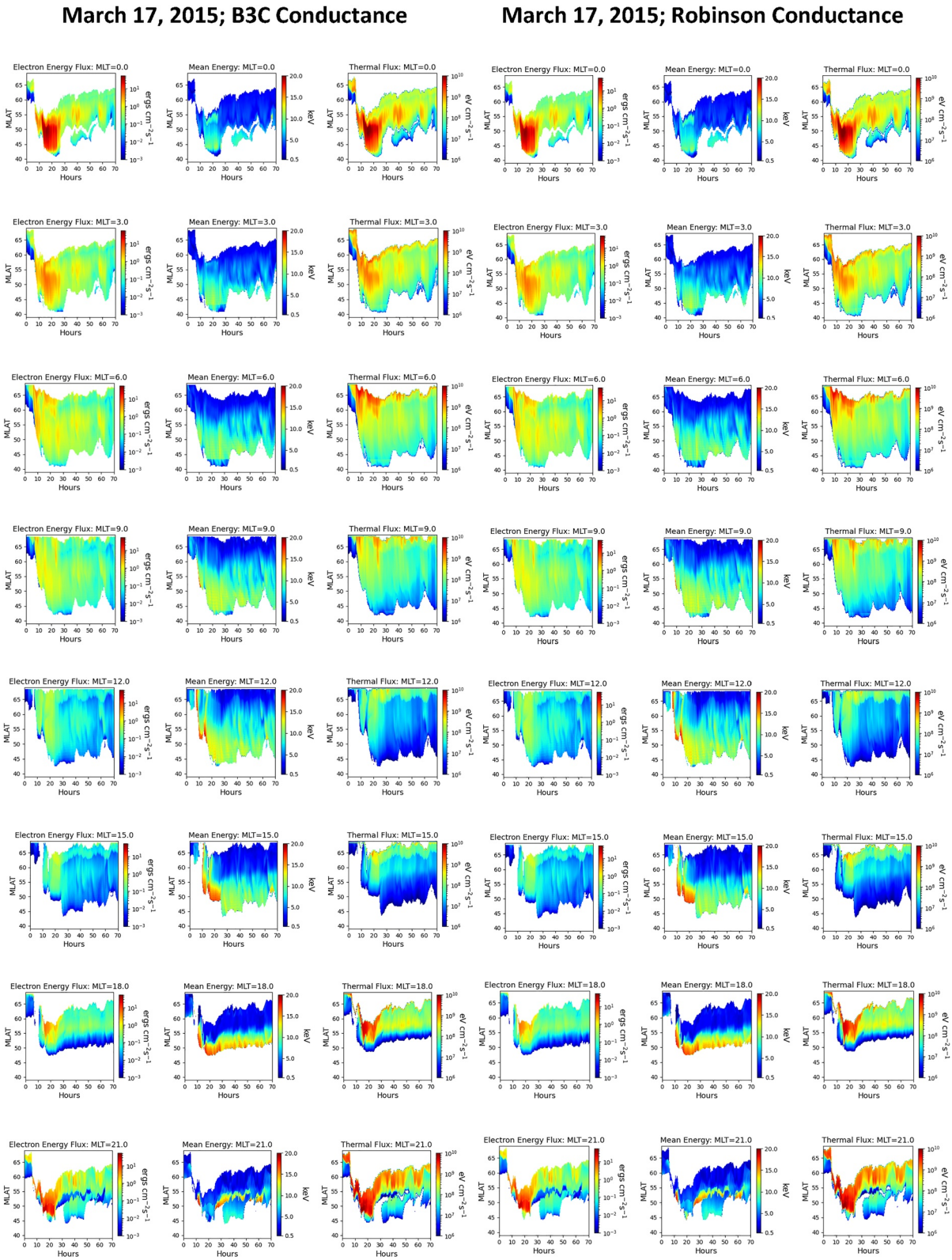

Figure 6. Geomagnetic storm 17 March 2015. RCM-E/STET-driven electron heat fluxes for selected MLTs and different height altitude-integrated conductances.

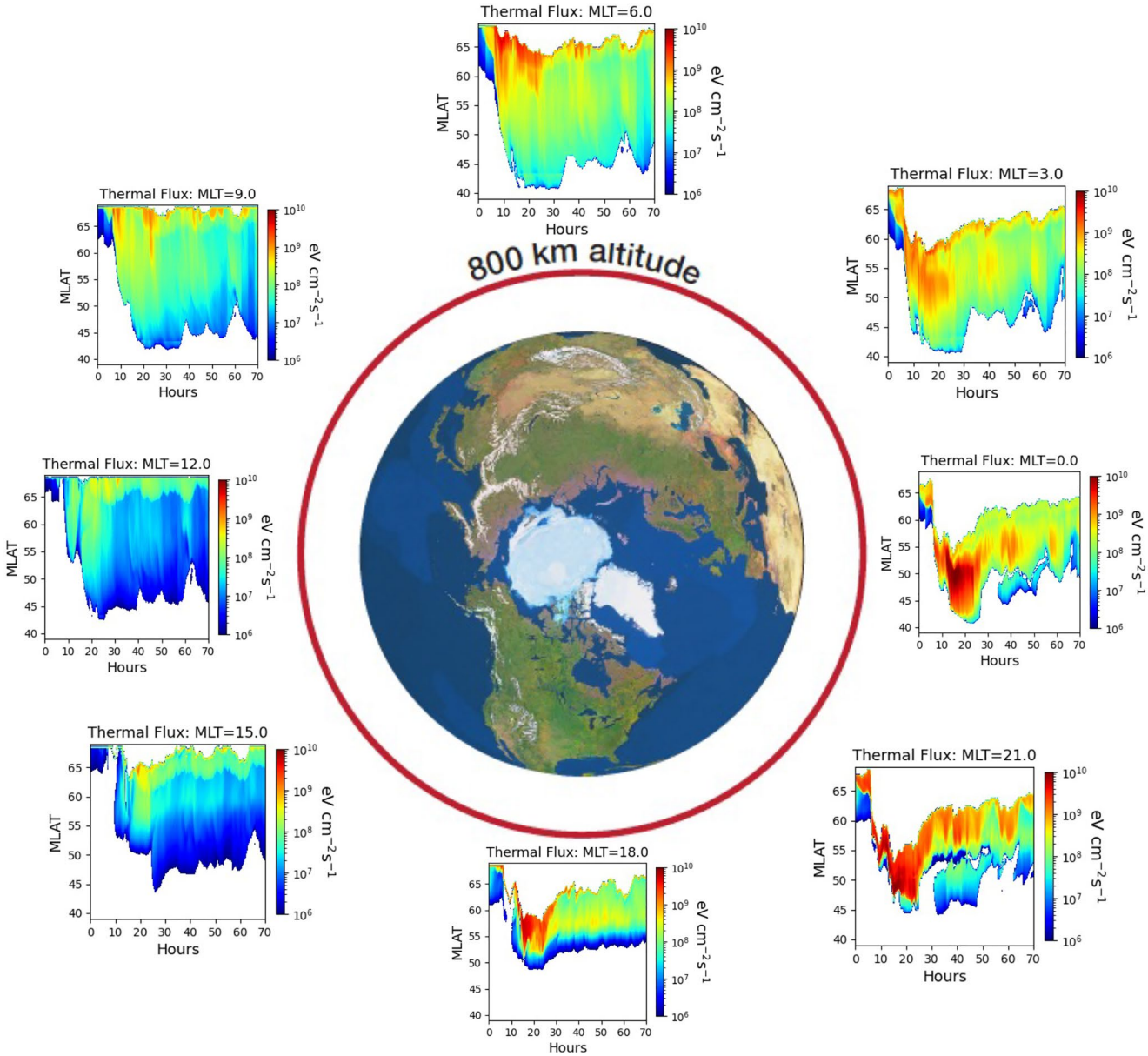

Figure 7. Clockwise MLTs electron heat fluxes development over the geomagnetic storm of 17–19 March 2015.

not necessarily identical approach we demonstrate in this manuscript would be required to represent the space weather simulations during magnetic storms and substorms.

Figure 8 shows the migration of maximum electron heat flux values in the region of diffuse aurora in the simulation MLAT/MLT domain of the RCM-E code, as the St. Patrick's Day 2015 geomagnetic storm develops. These electron thermal fluxes shown in affiliation with corresponding precipitation electron energy fluxes simulated by coupled RCM-E/STET code are much stronger and during the main phase of the storm exceed corresponding 2013 storm values almost by an order of magnitude.

As during St. Patrick's geomagnetic storm 2013, these two parameters are well correlated with each other and their MLAT and MLT locations have some of the noticeable differences in their MLT coverage. Compared to St. Patrick's geomagnetic storm 2013, both energy fluxes during 2015 storm have larger scattering over the MLAT and MLT simulation domains. That provides more energy to MIA coupling system that must be considered by ionospheric modeling networks. Blue and red lines and dots in windows of Figure 8 represent the different models of integrated ionospheric conductance that have been used in simulated scenario of RCM-E/STET coupled code.

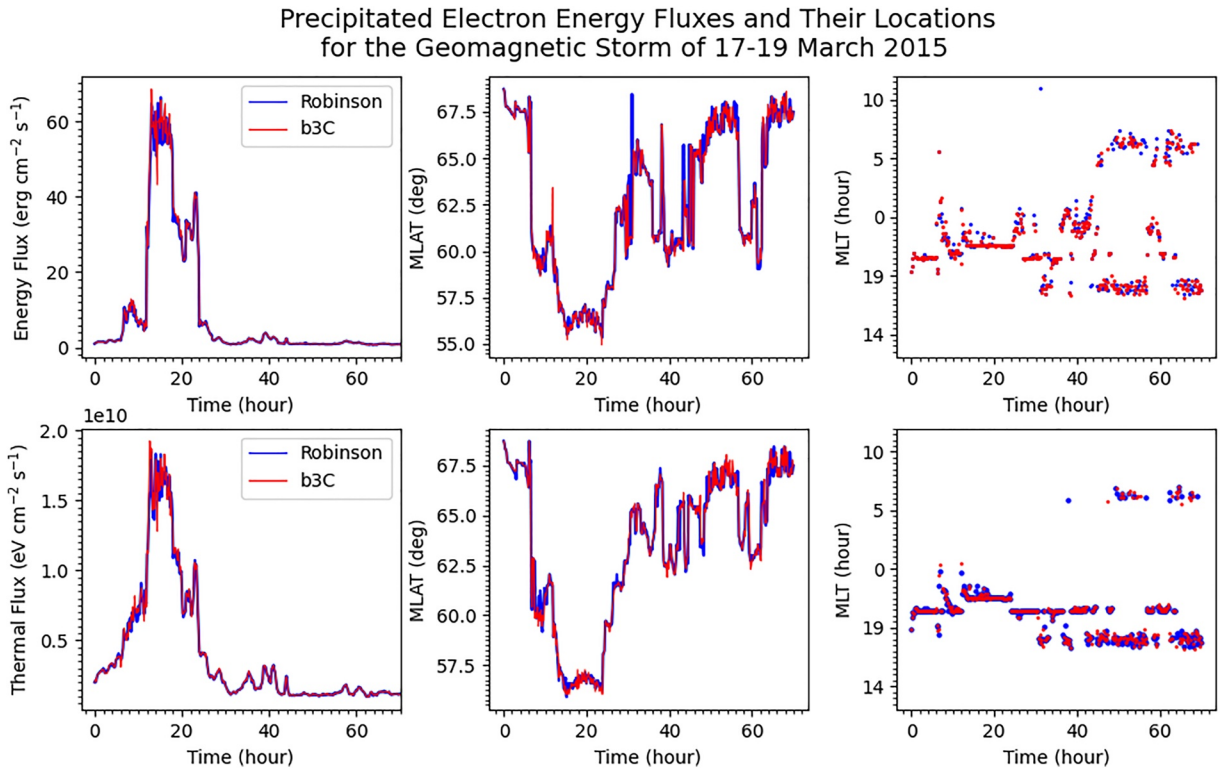

Figure 8. Maximum values of electron precipitation energy and heat fluxes migration over the geomagnetic storm of 17–19 March 2015.

As during the St. Patrick's 2013 storm, there are some differences in the locations of the parameters presented here that apparently are related to the electric field calculations and would be investigated in our future studies.

It should be noted that the results presented here show only these values that are associated with precipitated auroral electrons during St. Patrick's Days of 2013 and 2015 geomagnetic storms. As we have mentioned above, another systematic dayside source of the thermal electron heat fluxes is ionospheric photoelectrons that are resulted from the interaction of solar UV and X radiations with the neutral atmosphere (Khazanov, 2010). The contribution of this process in the overall analysis of the thermal electron heat flux formation during selected geomagnetic storms will be mentioned in the follow-up sections of this manuscript.

5. DMSP Observation During St. Patrick's 2013 and 2015 Storms: Data/Theory Validation

DMSP provides a comprehensive data set of multiple ionospheric parameters, but only those relevant to the problem considered in this paper are used in the studies presented below. The data selected below cover only the most disturbed period of St. Patrick's Days of 2013 and 2015 geomagnetic storms shown in Section 2 and presented and discussed in RCM-E/STET simulations in Sections 4.2 and 4.3.

5.1. Instrumentation

Three DMSP satellites - F16–F18 - provide data for this study. Each of the DMSP spacecraft is a three-axis stabilized satellite flying at altitude of ~840–850 km in circular, sun-synchronous polar (inclination 98.7°) orbit of about 100 min period. During the period of interest, the geographic local times of the orbits are near 18:00–06:00 (F16 and F17) and 21:00–09:00 (F18) meridians. Owing to the offset between the geographic and geomagnetic poles, the satellites sample a wide range of MLTs over the course of a day. The ascending nodes of DMSP orbits are on the dusk side of the Earth. Thus, the satellites move toward the northwest in the evening LT sector. In this study, we use the Special Sensor for Precipitating Particles (SSJ/5; Hardy et al., 1993) and the Topside Ionospheric Plasma Monitor (SSIES; Rich & Hairston, 1994).

Once per second, the SSJ/5 instrument measures electrons and ions with energies from 30 keV to 30 eV in 19 logarithmically spaced steps. The field of view is a 4° by 90° fan ranging from zenith to the horizon. The 90° field of view is divided into six 15° zones providing pitch angle distribution once per second. SSIES sensors are tailored to the anticipated environment at 840 km altitude and at all latitudes, all local times, all seasons, and all phases of the sunspot cycle. Of those, we use a spherical Langmuir probe to determine the temperature ($500 \leq T_e \leq 9000$ K) of ambient electrons once per 4 s with the nominal accuracy of ±200 K or ±10%. Note that additional errors in T_e can be caused by contamination of the Langmuir probe by photoelectrons or/and secondary, <100 eV, electrons if the local ambient density drops below $\sim 10^3$ cm^{-3}. These factors result in T_e data gaps that were excluded in the DMSP results presented below.

It should be also noted, that the MLAT and MLT values come from ephemeris data obtained using the model field along the orbit. The magnetic distortion during major storms, like those under study, leads to significant deviations from the model thus making the mapping between the magnetic equator to the ionosphere inaccurate. In other words, the actual values, especially near dusk, may significantly deviate from the model values (e.g., Tsyganenko et al., 2003). For example, Burke et al. (1998) found that the magnetic field is more inflated than magnetic field models indicated. This means that the model field line crosses the equatorial plane closer to the Earth than the actual field line, and that a given point in the magnetic equatorial plane maps to higher latitudes than it does in reality.

5.2. Selected DMSP Data in the Main Phase of the Storms: General Overview

5.2.1. Data on 17 March 2013

The approach that we developed to calculate electron heat fluxes is based on the knowledge of electron precipitated energy fluxes and their mean energies (Khazanov et al., 2022). These parameters are presented below in two upper panels of Figure 9 and measured by three DMSP satellites F16–F18 on 17 March between 9.8 and 15.2 UTs. Such selection of the time intervals is driven by RCM-E/STET simulation results presented in Figure 5 and corresponds to the most disturbed time of simulated electron precipitated fluxes and associated thermal electron heat fluxes.

Variations of the MLAT and MLT values of the ionospheric footpoints of F16–F18 along their trajectories are shown in two bottom panels of Figure 9. Energy spikes of precipitated electrons measured by the three satellites, shown in the upper panel of this figure, clearly correspond to the high MLAT values in the Northern and Southern Hemispheres and the evening and morning MLT sectors between 6 and 18 hr. Such a behavior is qualitatively consistent with that presented in RCM-E/STET simulated results shown in Figures 4 and 5.

5.2.2. Data on 17 March 2015

Similar to the data presented in the previous subsection, Figure 10 shows electron precipitated energy fluxes and their mean energies measured by F16 and F17, while the data from F18 were unavailable on 17 March 2015 between 12 and 15 UT. As in the case of the St. Patrick 2013 geomagnetic storm, this time interval was selected to represent the major disturbed period that was provided by RCM-E/STET simulations discussed in Section 4.2 and presented in Figures 6–8.

As above, variations of the MLAT and MLT values of the ionospheric footpoints of F16 and F17 along their trajectories are shown in two bottom panels of Figure 10. As in Figure 9, electron energy fluxes of precipitating electrons maximize near high MLAT in the Northern and Southern Hemispheres and their MLT extension is quite similar to that demonstrated in our simulation presented in Section 4.3. It should be noted, however, that all simulation results in Figures 6–8 correspond only to the northern hemisphere. Asymmetry analysis of electron precipitation fluxes formation and associated electron thermal fluxes will be considered in future RCM-E/STET simulations.

For both geomagnetic storms presented above in Figures 9 and 10, there is a clear tendency for dramatic drops in the electron energy fluxes at MLAT below approximately 50° in both hemispheres. Apparently, these locations represent the transitional boundary from the auroral to the subauroral latitudes.

6. Data/Theory Validation

The RCM-E/STET code electron heat flux calculation for the storm events will be validated in our manuscript using two different methods. First, we use DMSP F16–F18 observations of precipitating electron energy fluxes

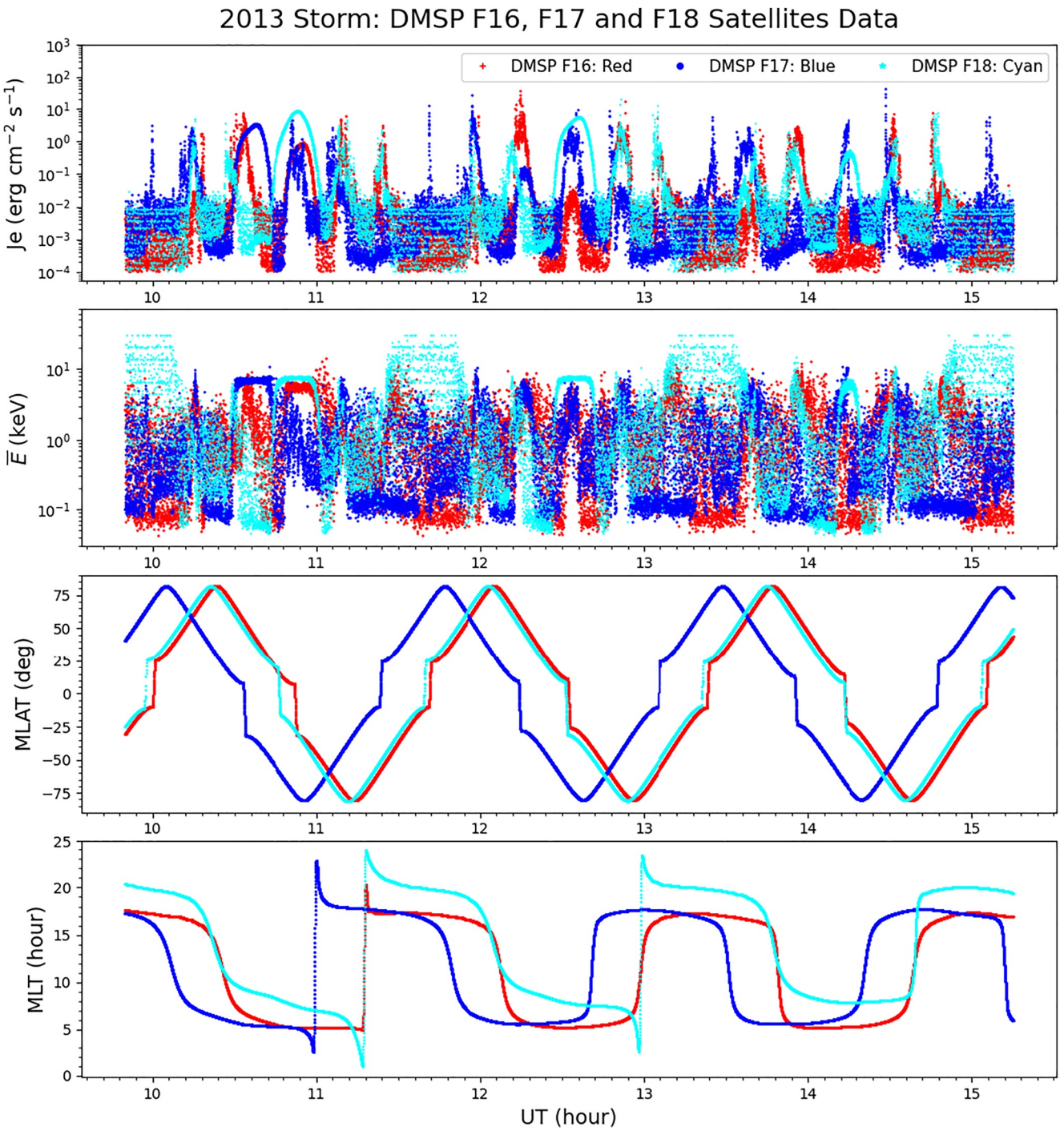

Figure 9. Defense Meteorological Satellite Program (DMSP) observation of the precipitated electron energy fluxes, their mean energies, and MLAT and MLT locations during the main phase of St. Patrick 2013 geomagnetic storm. See text for the details.

and their mean energy that are shown in Figures 9 and 10 to estimate the electron heat flux that correspond to these data. These thermal electron heat fluxes are calculated and presented in the upper panel of Figures 11 and 12. Further, we use these electron thermal heat flux estimations in an approach that is presented by Khazanov (2010) in Chapter 6 of that book to calculate the electron temperature and compare it with available DMSP Te data. These DMSP Te data also are shown as the second panel in Figures 11 and 12.

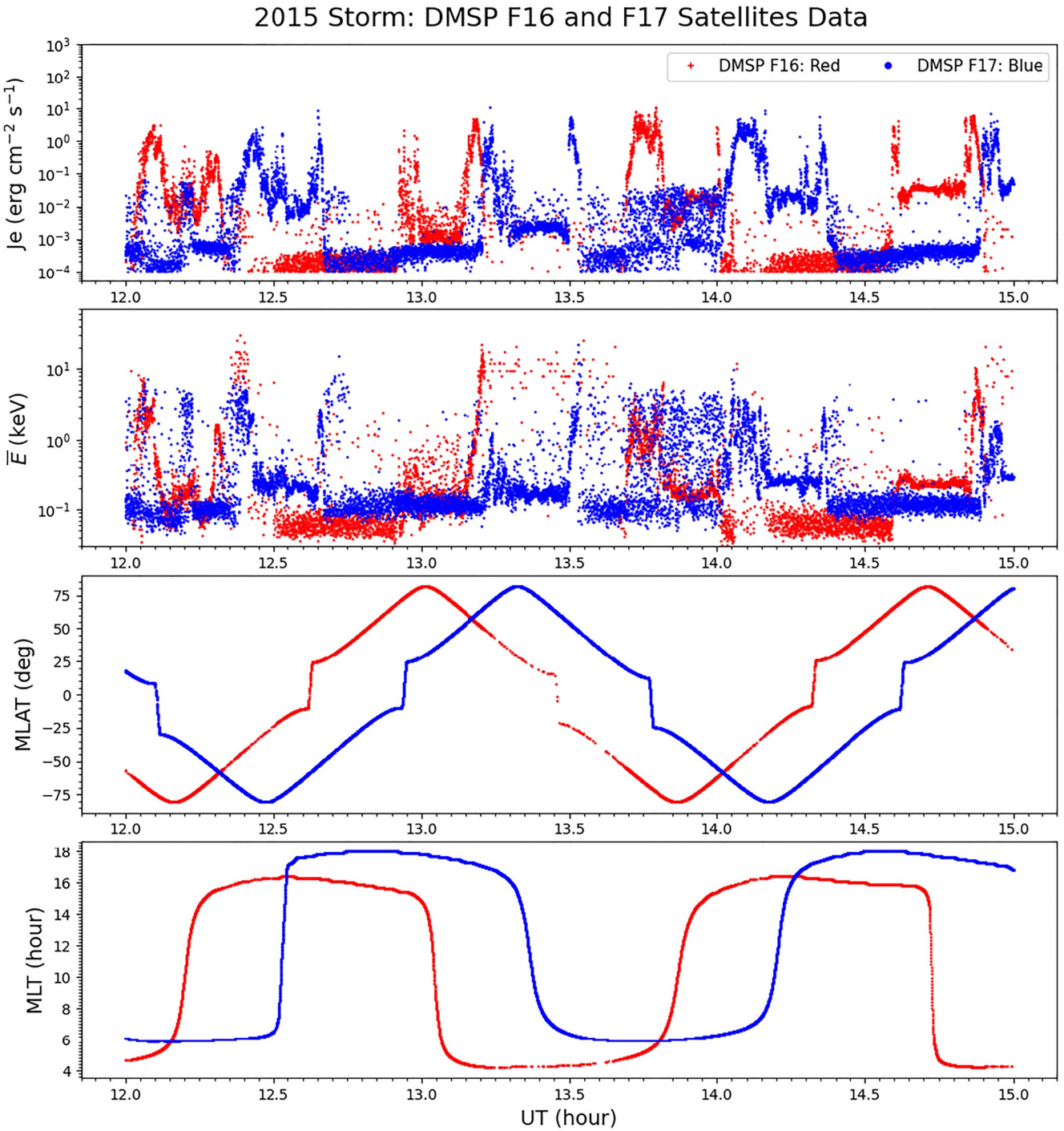

Figure 10. Defense Meteorological Satellite Program (DMSP) observation of the precipitated electron energy fluxes, their mean energies, and MLAT and MLT locations during the main phase of St. Patrick 2015 geomagnetic storm. See text for details.

Second, we will use our theoretical RCM-E/STET based electron thermal flux calculation shown in Figures 4–8 to estimate the electron temperatures during the St. Patrick's Days 2013 and 2015 geomagnetic storms and discuss their correspondence to DMSP Te observations. Here the focus is on the most disturbed time period. As in the first model-data validation approach, these data will be presented at the locations where electron precipitation electron thermal heat fluxes dominate over the heat fluxes that are coming from the ionospheric photoelectrons.

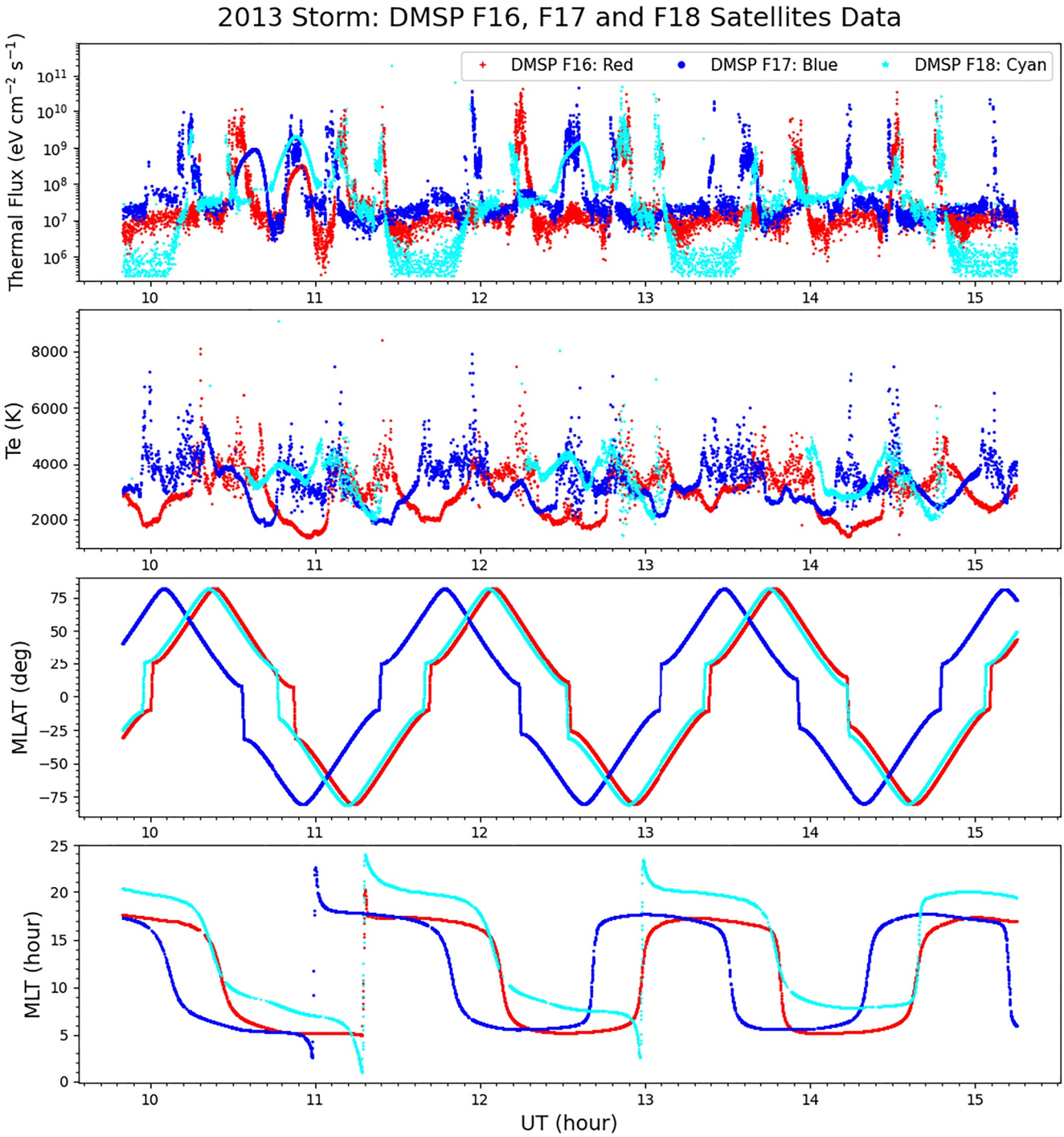

Figure 11. Defense Meteorological Satellite Program (DMSP)-based electron thermal fluxes calculation and their comparison with the measured electron temperatures during the St. Patrick 2013 geomagnetic storm. See text for the details.

6.1. DMSP Based Electron Heat Fluxes

The top panel of Figure 11 shows the electron heat flux calculated using the DMSP precipitating electron energy fluxes and mean energies and the STET code-based methodology of electron thermal flux calculation for the St. Patrick's Storm 2013. The second upper panel in Figure 11 shows the electron temperature measurements from the DMSP satellites. The last two panels in Figure 11 show the MLAT and MLT locations of the parameters discussed above.

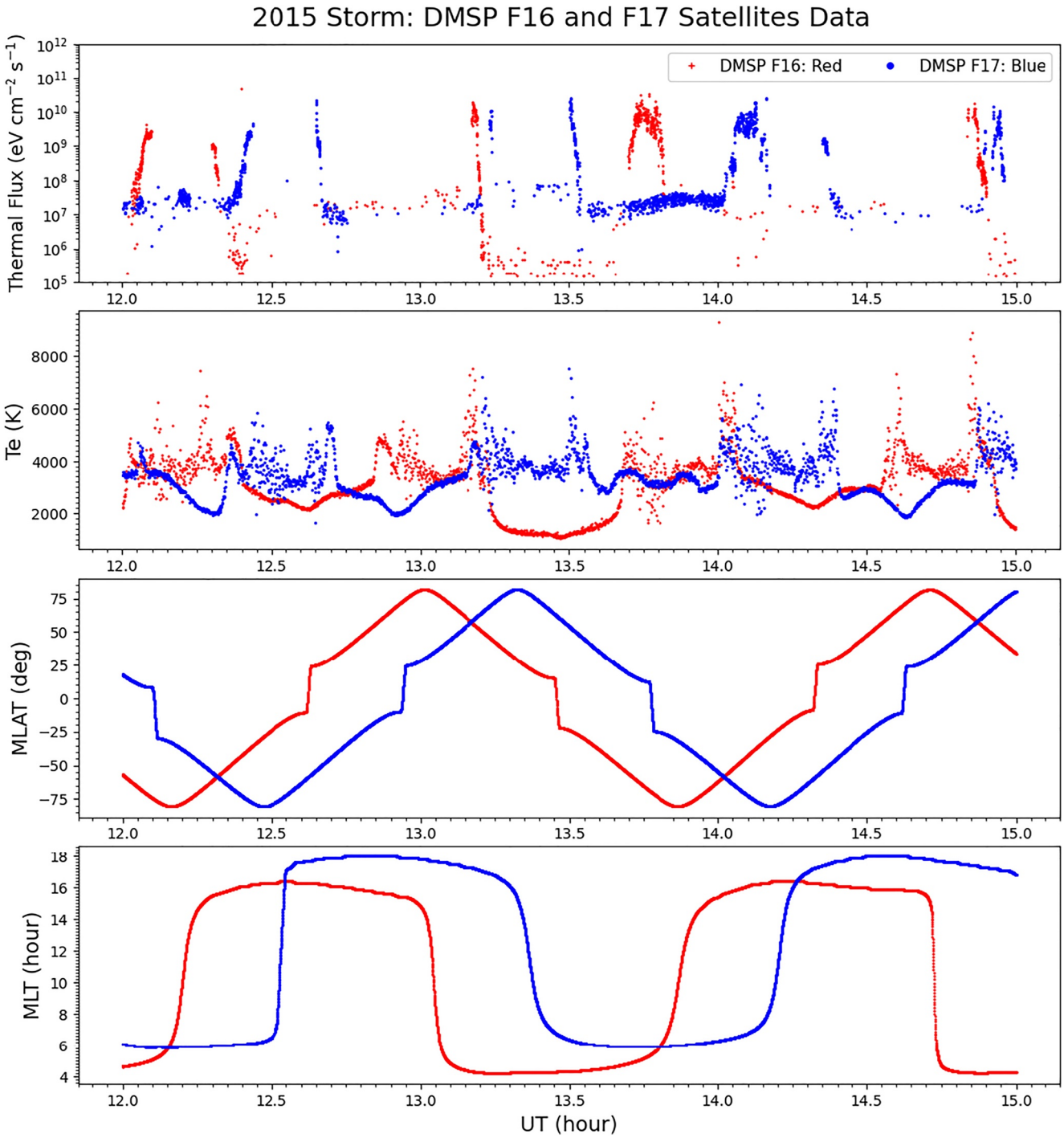

Figure 12. Defense Meteorological Satellite Program (DMSP)-based electron thermal fluxes calculation and their comparison with the measured electron temperatures during the St. Patrick 2015 geomagnetic storm. See text for the details.

The same format as above is used for the analysis of the St. Patrick 2015 storm presented in Figure 12. Here we used data from F16 and F17 only because the F18 data were not available on 17 March 2015 during the 12:00–16:00 UT interval. Compared to the 17 March 2013 geomagnetic storm, the number of points corresponding to the measurements of F16 and F17 is visibly fewer than for the St. Patrick's 2015 storm. Apparently, the DMSP data selection criteria that we briefly discussed in Section 5.1 have limited data accuracy for such a strong geomagnetic storm as occurred on 17 March 2015. Therefore, the majority of the DMSP data were not available for the detailed analysis of data-theory comparison.

Table 1
The Relation Between Electron Temperatures, T_e, and Electron Heat Fluxes, Q_T

Q_T	eV*cm^{-2}*s^{-1}	5×10^7	10^8	5×10^8	10^9	5×10^9	10^{10}	5×10^{10}	10^{11}	5×10^{11}
T_e	K degree	1190	1450	2297	2800	4434	5406	8562	10437	16530

Because the major focus of our paper is the thermal electron heat fluxes associated with precipitated *auroral* electrons during St. Patrick's Days of 2013 and 2015 geomagnetic storms, most of the attention here is on the high latitudinal *auroral* regions, above 50° MLAT, where electron precipitation sources dominate over other thermal electron heating mechanisms. Looking at high MLAT and corresponding MLT where electron precipitation intensifies, one can see the visible correlation between the electron heat fluxes and corresponding electron temperatures. Do these parameters correspond to each other at the DMSP altitudes of 840–850 km?

Table 1 presents the relation between electron temperatures, T_e, and electron heat fluxes, Q_T, at the upper ionospheric altitudes determined in Chapter 6 of the Khazanov (2010) book. In comparison with this publication, Table 1 is adjusted to DMSP altitudes and extended to a broader range of the heat flux values to give the readers benchmarks in the data analysis considered below.

At the DMSP altitudes, electron heat fluxes form in less than 3 min (Khazanov, Ma, & Chu, 2022), and the electron temperature almost instantly responds to their variations (Khazanov et al., 2022) because energy losses at these altitudes are negligible (Khazanov, 2010). The last statements are equally applicable for the Northern and Southern Hemispheres. Therefore, examples in Table 2, which is based on results presented in Figures 11 and 12, are given for electron temperatures measured in both hemispheres by F16–F18.

It should be noted that DMSP electron temperature measurements are resolved on the time scale of 4 s and are shown in the second top windows of Figures 11 and 12. In Table 2, this actual Te measurement is indicated as Te/DMSP. That is why the analysis presented in Table 2 is done using DMSP-based heat flux calculations presented in the upper windows of Figures 11 and 12, and was also, for consistency, averaged over the same time scale before Te/DMSP and Te/DMSP-STET-based data are compared to each other.

As it is shown in Table 2, Te/DMSP and Te/DMSP-STET-based data are very close to each other within 10% difference. This is consistent with the error of Te observations by DMSP satellites and ensures the validity of heat flux calculation technique presented in this paper.

6.2. RCM-E/STET Versus DMSP-Observation

As we mentioned in Section 4.2, the RCM-E code computes the bounce-averaged guiding-center drift motion of isotropic ions and electrons in the closed field line region of the magnetosphere (Toffoletto et al., 2003; Wolf, 1983) and the results presented in Figures 4–8 are shown with the time step of 10 min. Correspondingly, compared to the first type of Data/Theory validation presented in Section 6.1, direct comparison of Te that are driving RCM-E/STET theoretical heat fluxes is simply not representative, because it requires averaging DMSP Te observation over the time interval of 10 min. During this time, DMSP satellites cover the distance of several thousand kilometers, and such Data/Theory will not be accurate and clear.

Figures 13 and 14 illustrate Te calculation at the altitude of 850 km using theoretical electron heat fluxes driven by RCM-E/STET simulations and presented for the St. Patrick 2013 storm in Figure 5 and for the corresponding 2015 storm in Figure 8. These heat fluxes are shown in the first row of Figures 13 and 14 and cover entire development of both geomagnetic storms. Correspondingly, the second row of this figure presents electron temperature calculation using an approach that is utilized by Khazanov (2010, Chapter 6). These electron temperature calculations are resolved, as corresponding RCM-E/STET simulation on the time scale of 10 min, and the analysis of these results can be done only in a qualitative way.

As is shown in Figures 13 and 14, electron heat fluxes and corresponding Te are well correlated for both geomagnetic storms. During the main phase of the 17 March 2013 storm the maxima of electron temperature vary from 3500 to 4500 K degrees, and, correspondingly, for the 2015 geomagnetic storm such values are from 5000 to 6500 K degrees. Electron temperature calculations for both geomagnetic storms only slightly depend on the RCM-E/STET integrated conductance model, and, in general and only qualitatively, during the main phases of the storm correlated with DMSP observations.

Table 2
Comparison Te/DMSP and Te/DMSP-STET-Based Data

St. Patrick Day 2013 geomagnetic storm					
			F16		
UT	10.50	11.20	12.25	13.9	14.55
MLAT	65.00	−80.12	55.20	65.53	−75.00
MLT	07.00	05.00	07.25	06.20	05.75
Te/DMSP	5,750	5,636	7,100	5,050	6,020
Te/DMSP-STET	5,695	5,670	7,400	5,025	6,590
			F17		
UT	10.20	11.10	11.95	13.43	14.25
MLAT	61.00	−52.50	49.50	65.50	70.10
MLT	07.50	18.50	6.53	17.00	6.50
Te/DMSP	5,050	6,800	8,051	6,110	7,050
Te/DMSP-STET	4,900	6,394	8,033	6,590	6,570
			F18		
UT	10.25	11.20	12.85	14.55	14.80
MLAT	64.85	−75.00	−75.00	−65.00	−51.50
MLT	18.55	5.05	7.00	07.07	20.00
Te/DMSP	NA	5,200	6,400	4,900	6,050
Te/DMSP-STET	4,240	5,072	6,590	4,750	6,500
St. Patrick Day 2015 geomagnetic storm					
			F16		
UT	12.05	13.20	13.75	14.90	
MLAT	−61.00	50.50	−65.00	51.00	
MLT	03.00	2.50	05.00	02.00	
Te/DMSP	4,300	7,050	5,800	8,010	
Te/DMSP-STET	4,100	6,750	5,405	7,400	
			F17		
UT	12.40	13.25	14.10	14.95	
MLAT	−67.00	65.50	−68.00	70.00	
MLT	06.20	16.50	06.20	17.50	
Te/DMSP	4,010	5,760	6,010	6,030	
Te/DMSP-STET	4,100	6,200	6,069	5,500	

7. Concluding Remarks

Electron thermal heat flux is an important parameter for the global ionospheric modeling networks. This parameter is not measurable explicitly by any of existing space plasma techniques and usually is selected based on the limited comparison of simulated electron temperature results with observations (Fallen & Watkins, 2013; Schunk et al., 1986). Such observations are not available on the global scale, especially in the cases of ionospheric and magnetospheric disturbances - geomagnetic storms and substorms.

Recently we developed a rigorous approach to the calculation of electron heat fluxes reaching the topside ionosphere in various regions including the polar cap (Khazanov, Chen, et al., 2019), diffuse aurora (Khazanov et al., 2020), and discrete aurora (Khazanov, Glocer, & Chu, 2021). Using approaches presented in these papers and utilizing the 2D array of Time History of Events and Macroscale Interactions all-sky-imager (ASI) observations by Gabrielse et al. (2021) during this Substorm, Khazanov et al. (2022) obtained the electron thermal

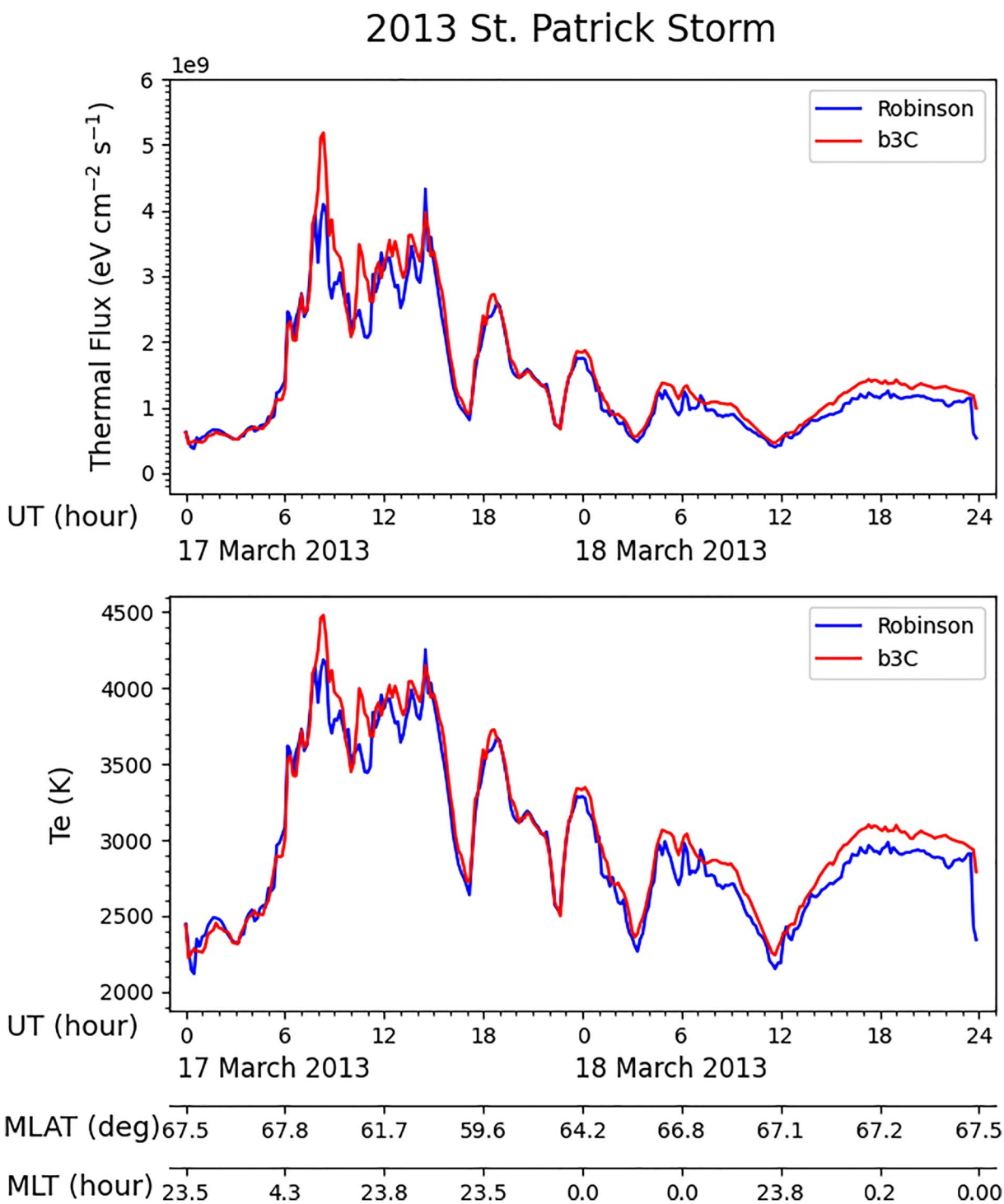

Figure 13. Geomagnetic storm 17 March 2013. RCM-E/STET-driven electron heat fluxes and the corresponding temperature calculation. MLAT and MLT locations are shown in axes below.

heat fluxes during two substorms on 16 February 2010 and validated these results using electron temperature observation at Alaska, Poker Flat, from Incoherent Scatter Radar data. The Supporting Information presented by Khazanov et al. (2022) in this paper have demonstrated that the proposed methodology for the calculation of the heat flux is reasonable when compared to the observations within the limitations of the electron temperature observations.

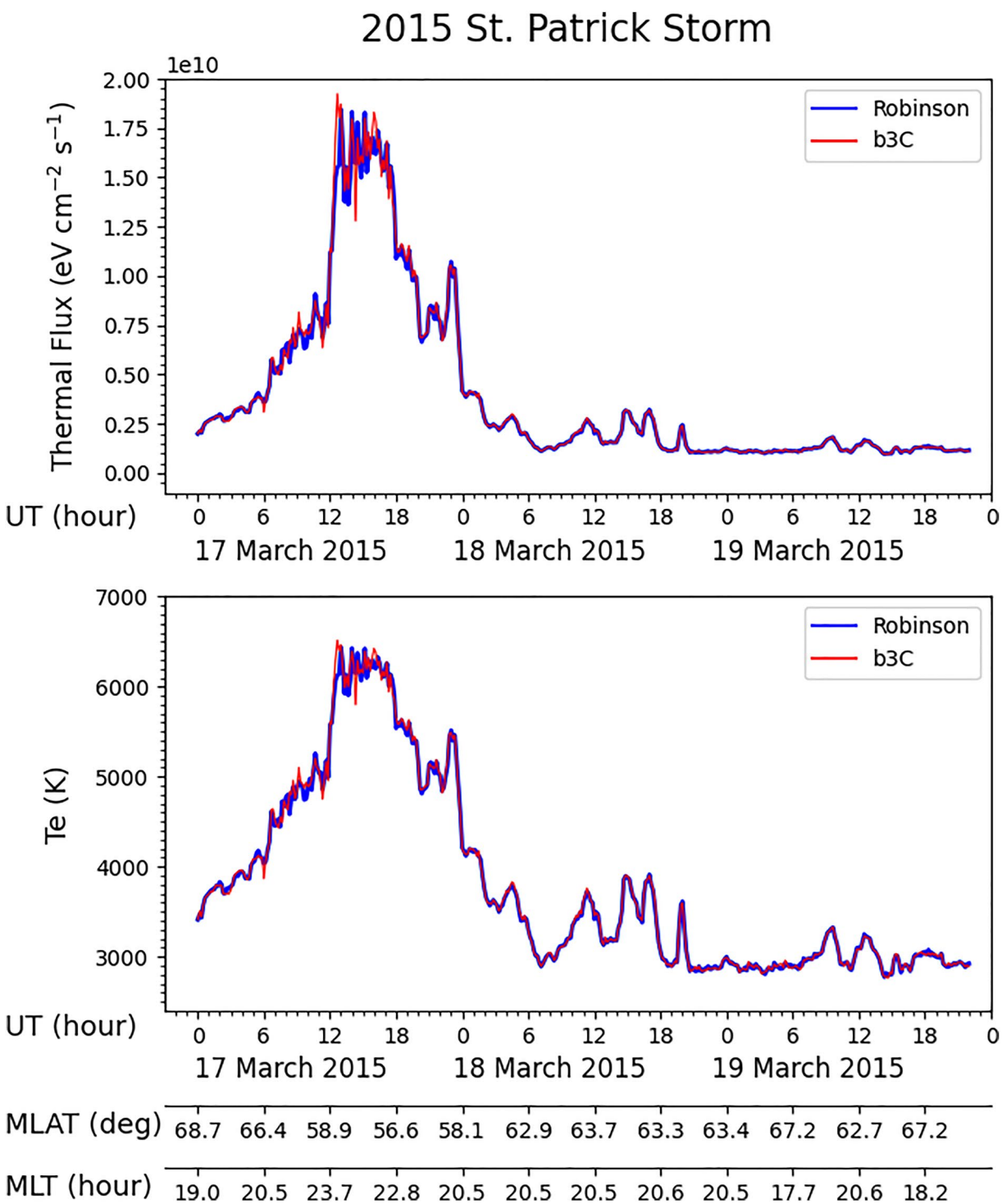

Figure 14. Geomagnetic storm 17 March 2015. RCM-E/STET-driven electron heat fluxes and the corresponding temperature calculation. MLAT and MLT locations are shown in axes below.

This paper analyzes the thermal electron heat flux formation during the most disturbed magnetospheric conditions, but on the global scale, and using precipitated auroral electrons during Saint Patrick's 2013 and 2015 Geomagnetic Storms. Selection of these precipitated electron fluxes were done using corresponding data coming from RCM-E/STET model simulations and DMSP observations with major emphasis on the main phases of these

geomagnetic storms. Precipitated electron energy fluxes and their mean energies from these two independent sources are further adapted in the STET code for the estimation of thermal electron heat fluxes and the corresponding electron temperatures.

One of the most important issues in the analysis of above-presented results was the appropriate selection of magnetospheric energy input to the STET code for the estimations of the thermal electron heat fluxes. In this sense, the choice of DMSP electron energy fluxes and their mean energies observations from the F16–F18 satellites and follow-up evaluation of the electron thermal heat fluxes is an ideal case, because, besides these values this mission provides the electron temperature observation that at the DMSP altitudes is defined by electron heat fluxes. From the other hand, the selection of RCM-E in our analysis presented above was very instrumental to study the quantitative and qualitative relation between electron precipitation and electron heat flux formation on the global scale because the DMSP satellites orbits are only Sun-synchronous ones.

The thermal electron heat fluxes calculations that are presented in this paper during the Saint Patrick's 2013 and 2015 Geomagnetic Storms correspond to the region of diffuse aurora only, because the RCM-E is developed (Chen et al., 2019) and applied in the combination with the STET code (Khazanov, Chen et al., 2019) only for this part of the region. Additional development of RCM-E code is required to handle other types of auroral physics. STET code includes the region of the discrete aurora (Khazanov, Glocer, & Chu, 2021), but also needs to be improved for the analysis of arbitrary electron precipitation function that corresponds to the region of Alfven and other auroras.

With all restrictions of our analysis that we discussed above, for the first time, the electron thermal flux formation is presented and analyzed on the global scale when intense electron precipitations occur during the Saint Patrick's 2013 and 2015 Geomagnetic Storms (see Figures 4–8 and affiliated discussions in the text). We validated electron heat fluxes results in this manuscript by comparing our simulation with the DMSP F16–F18 satellites observations (see Figures 9–12 and Table 2 for details) and general analysis of electron temperature development presented in Figures 13 and 14 that is based on RCM-E/STET coupled simulations.

As it is presented in Table 2, Te/DMSP and Te/DMSP-STET-based data are very close to each other within 10% difference. This is consistent with the uncertainty of Te observations by DMSP satellites and ensures the validity of heat flux calculation technique presented in this paper.

Data Availability Statement

The data used in this study are available at https://zenodo.org/record/7379528.

Acknowledgments

The authors thank Colby Lemon for discussions on the RCM-E and J. Scott Evans for providing look up tables of B3C conductances. G. V. K. was supported by NASA HTMS program under award of 80NSSC20K1276, the MARBLE Project, funded by the NASA Living with a Star (LWS) Strategic Capabilities program, LWS Program under the awards 80NSSC19K0080 and 80NSSC20K1817, NASA award 80NSSC21K1552, NASA award 80NSSC21K1552 and the Comprehensive Auroral Precipitation Experiment (CAPE) on NASA's Geospace Dynamics Constellation (GDC) mission as part of the Living With a Star (LWS) program. M. W. C. was supported by the NSF grant AGS 225404, NASA awards 80NSSC21K1552 and NNH19ZDA001N-HGIO, and the Aerospace Technical Investment Program. E. V. M. was supported by the Air Force Office of Scientific Research LRIR 22RVCOR011. The DMSP data used in the study were obtained from the NOAA-website (https://satdat.ngdc.noaa.gov/dmsp/data/).

References

Banks, P. (1966). Charged particle temperatures and electron thermal conductivity in the upper atmosphere. *Annales Geophysicae*, *22*, 557–587.

Basu, B., Jasperse, J. R., Strickland, D. J., & Danielle, R. E., Jr. (1992). Transport-theoretic model for the electron-proton-hydrogen atom aurora: 1. Theory. *Journal of Geophysical Research*, *98*(A12), 98–21532. https://doi.org/10.1029/93JA01646

Bekerat, H. A., Schunk, R. W., & Scherliess, L. (2007). Estimation of the high-latitude topside electron heat flux using DMSP plasma density measurements. *Journal of Atmospheric and Solar-Terrestrial Physics*, *69*(9), 1029–1048. https://doi.org/10.1016/j.jastp.2007.03.015

Bilitza, D., Altadill, D., Truhlik, V., Shubin, V., Galkin, I., Reinisch, B., & Huang, X. (2017). International reference ionosphere 2016: From ionospheric climate to real-time weather predictions. *Space Weather*, *15*(2), 418–429. https://doi.org/10.1002/2016SW001593

Bilitza, D., & Reinisch, B. W. (2008). International Reference Ionosphere 2007: Improvements and new parameters. *Advances in Space Research*, *42*(4), 599–609. https://doi.org/10.1016/j.asr.2007.07.048

Burke, W. J., Maynard, N. C., Hagan, M. P., Wolf, R. A., Wilson, G. R., Gentile, L. C., et al. (1998). Electrodynamics of the inner magnetosphere observed in the dusk sector by CRRES and DMSP during the magnetic storm of 4–6 June 1991. *Journal of Geophysical Research: Space Physics*, *103*(A12), 29399–29418. https://doi.org/10.1029/98JA02197

Case, N. A., & MacDonald, E. A. (2015). Aurorasaurus and the St Patrick's Day storm. *Astronomy and Geophysics*, *56*(3), 3-13–3.14. https://doi.org/10.1093/astrogeo/atv089

Chen, M. W., Lemon, C. L., Guild, T. B., Schulz, M., Roeder, J. L., & Le, G. (2012). Comparison of self-consistent simulations with observed magnetic field and ion plasma parameters in the ring current during the 10 August 2000 magnetic storm. *Journal of Geophysical Research*, *117*(A9), A09232. https://doi.org/10.1029/2012JA017788

Chen, M. W., Lemon, C. L., Hecht, J., Sazykin, S., Wolf, R. A., Boyd, A., & Valek, P. (2019). Diffuse auroral electron and ion precipitation effects on RCM-E comparisons with satellite data during the 17 March 2013 storm. *Journal of Geophysical Research: Space Physics*, *124*(6), 4194–4216. https://doi.org/10.1029/2019JA026545

Chen, M. W., Lemon, C. L., Orlova, K., Shprits, Y., Hecht, J., & Walterscheid, R. L. (2015). Comparison of simulated and observed trapped and precipitating electron fluxes during a magnetic storm: Simulated and observed electron fluxes. *Geophysical Research Letters*, *42*(20), 8302–8311. https://doi.org/10.1002/2015GL065737

Cole, K. D. (1965). Stable auroral red arcs, sinks for energy of *Dst* main phase. *Journal of Geophysical Research*, *70*(7), 1689–1706. https://doi.org/10.1029/JZ070i007p01689

Cornwall, J. M., Coroniti, F. V., & Thorne, R. M. (1971). Unified theory of SAR arc formation at the plasmapause. *Journal of Geophysical Research*, *76*(19), 4428–4445. https://doi.org/10.1029/JA076i019p4428

Curtis, S. A., Hoegy, W. R., Brace, L. H., & Winningham, J. D. (1985). Cusp altitudinal electron temperature gradient: Dynamics Explorer 2 implications for heating mechanisms. *Journal of Geophysical Research*, *90*(A5), 4415–4419. https://doi.org/10.1029/JA090iA05p04415

Fallen, C. T., & Watkins, B. J. (2013). Diurnal and seasonal variation of electron heat flux measured with the Poker Flat Incoherent-Scatter Radar. *Journal of Geophysical Research: Space Physics*, *118*(8), 5327–5332. https://doi.org/10.1002/jgra.50485

Fontaine, D., & Blanc, M. (1983). A theoretical approach to the morphology and the dynamics of diffuse auroral zones. *Journal of Geophysical Research*, *88*(A9), 7171–7184. https://doi.org/10.1029/JA088iA09p07171

Fontheim, E., Brace, L., & Winningham, J. (1987). Properties of low-energy electron precipitation in the cleft during periods of unusually high ambient electron temperatures. *Journal of Geophysical Research*, *92*(A11), 12267–12273. https://doi.org/10.1029/JA092iA11p12267

Fuller-Rowell, T. J., & Evans, D. (1987). Height-integrated Pedersen and Hall conductivity patterns inferred from TIROS-NOAA satellite data. *Journal of Geophysical Research*, *92*(A7), 7606–7618. https://doi.org/10.1029/JA092iA07p07606

Gabrielse, C., Nishimura, T., Chen, M., Hecht, J. H., Kaeppler, S. R., Gillies, D. M., et al. (2021). Estimating precipitating energy flux, average energy, and Hall auroral conductance from THEMIS all-sky-imagers with focus on mesoscales. *Frontiers in Physics*, *9*, 744298. https://doi.org/10.3389/fphy.2021.744298

Galand, M., & Richmond, A. D. (2001). Ionospheric electrical conductances produced by auroral proton precipitation. *Journal of Geophysical Research*, *106*(A1), 117–125. https://doi.org/10.1029/1999JA002001

Ginet, G. P., O'Brien, T. P., Huston, S. L., Johnston, W. R., Guild, T. B., Friedel, R., et al. (2013). AE9, AP9, and SPM: New models for specifying the trapped energetic particle and space plasma environment. *The Van Allen Probes Mission*, 579–615. https://doi.org/10.1007/978-1-4899-7433-4_18

Glocer, A., Khazanov, G., & Liemohn, M. (2017). Photoelectrons in the quiet polar wind. *Journal of Geophysical Research: Space Physics*, *122*(6), 6708–6726. https://doi.org/10.1002/2017JA024177

Glocer, A., Kitamura, N., Toth, G., & Gombosi, T. (2012). Modeling solar zenith angle effects on the polar wind. *Journal of Geophysical Research*, *117*(A4), A04318. https://doi.org/10.1029/2011JA017136

Hardy, D. A., Walton, D. M., Johnstone, A. D., Gough, M. P., Huber, A., Pantazis, J., & Burkhardt, R. (1993). The low energy plasma analyzer. *IEEE Transactions on Nuclear Science*, *40*(2), 246–251. https://doi.org/10.1109/23.212349

Hasegawa, A., & Mima, K. (1978). Anomalous transport produced by kinetic Alfven wave turbulence. *Journal of Geophysical Research*, *83*(A3), 1117–1123. https://doi.org/10.1029/JA083iA03p01117

Hedin, A. E. (1991). Extension of the MSIS thermospheric model into the middle and lower atmosphere. *Journal of Geophysical Research*, *96*(A2), 1159–1172. https://doi.org/10.1029/90JA02125

Johnstone, A. D., Walton, D. M., Liu, R., & Hardy, D. A. (1993). Pitch angle diffusion of low-energy electrons by whistler mode waves. *Journal of Geophysical Research*, *98*(A4), 5959–5967. https://doi.org/10.1029/92JA02376

Kataoka, R., Shiota, D., Kilpua, E., & Keika, K. (2015). Pileup accident hypothesis of magnetic storm on 17 March 2015. *Geophysical Research Letters*, *42*(13), 5155–5161. https://doi.org/10.1002/2015GL064816

Khazanov, G. V. (1979). *The kinetics of the electron plasma component of the upper atmosphere, Nauka, Moscow*. National Translation Center. English translation: #80-50707. 1980.

Khazanov, G. V. (2010). Kinetic theory of inner magnetospheric plasma. In *Astrophysics and space science library* (Vol. 372, p. 584). Springer Science & Business Media.

Khazanov, G. V., & Chen, M. W. (2021). Why atmospheric backscatter is important in the formation of electron precipitation in the diffuse aurora. *Journal of Geophysical Research: Space Physics*, *126*(5), e2021JA029211. https://doi.org/10.1029/2021JA029211

Khazanov, G. V., Chen, M. W., Lemon, C. L., & Sibeck, D. G. (2019). The magnetosphere-ionosphere electron precipitation dynamics and their geospace consequences during the 17 March 2013 storm. *Journal of Geophysical Research: Space Physics*, *124*(8), 6504–6523. https://doi.org/10.1029/2019JA026589

Khazanov, G. V., Gabrielse, C., Glocer, A., Chu, M., Nishimura, Y., & Reyes, P. (2022). A 2D kaleidoscope of electron heat fluxes driven by auroral electron precipitation. *Geophysical Research Letters*, *49*(18), e2022GL100912. https://doi.org/10.1029/2022GL100912

Khazanov, G. V., Gamayunov, K. V., Gallagher, D. L., Kozyra, J. U., & Liemohn, M. W. (2007). Self-consistent model of magnetospheric ring current and propagating electromagnetic ion cyclotron waves: 2. Wave-induced ring current precipitation and thermal electron heating. *Journal of Geophysical Research*, *112*(A4), A04209. https://doi.org/10.1029/2006JA012033

Khazanov, G. V., Glocer, A., & Chu, M. (2020). The formation of electron heat flux in the region of diffuse aurora. *Journal of Geophysical Research: Space Physics*, *125*(8), e2020JA028175. https://doi.org/10.1029/2020JA028175

Khazanov, G. V., Glocer, A., & Chu, M. (2021). Electron energy interplay in the geomagnetic trap below the auroral acceleration region. *Journal of Geophysical Research: Space Physics*, *126*(5), e2020JA028811. https://doi.org/10.1029/2020JA028811

Khazanov, G. V., Glocer, A., & Himwich, E. W. (2014). Magnetosphere-ionosphere energy interchange in the electron diffuse aurora. *Journal of Geophysical Research: Space Physics*, *119*(1), 171–184. https://doi.org/10.1002/2013JA019325

Khazanov, G. V., Himwich, E. W., Glocer, A., & Sibeck, D. (2016). Role of multiple atmospheric reflections in formation of electron distribution function in the diffuse aurora region. Auroral dynamics and space weather. *Geophysical Monograph Series*, *215*, 115–130. https://doi.org/10.1002/9781118978719

Khazanov, G. V., Ma, Q., & Chu, M. (2022). Electron heat fluxes generated by intense whistler waves at the upper ionospheric altitudes. *Journal of Geophysical Research: Space Physics*, *127*(9), e2022JA030753. https://doi.org/10.1029/2022JA030753

Khazanov, G. V., Robinson, R. M., Zesta, E., Sibeck, D. G., Chu, M., & Grubbs, G. A. (2018). Impact of precipitating electrons and magnetosphere-ionosphere coupling processes on ionospheric conductance. *Space Weather*, *16*(7), 829–837. https://doi.org/10.1029/2018SW001837

Khazanov, G. V., Shen, Y., Vasko, I. Y., Artemyev, A. V., & Chu, M. (2021). Magnetosphere-ionosphere coupling of precipitated electrons in diffuse aurora driven by time domain structures. *Geophysical Research Letters*, *48*(10), e2021GL092655. https://doi.org/10.1029/2021GL092655

Khazanov, G. V., Sibeck, D. G., & Chu, M. (2021). Magnetosphere-ionosphere coupling of precipitating electrons and ionospheric conductance, space physics and aeronomy collection volume 2. In R. Maggiolo, N. André, H. Hasegawa, D. T. Welling, Y. Zhang, & L. J. Paxton (Eds.), *Magnetospheres in the solar system, geophysical monograph* (Vol. 259, 1st ed.). John Wiley & Sons, Inc. https://doi.org/10.1002/9781119507512

Khazanov, G. V., Sibeck, D. G., & Zesta, E. (2017). Major pathways to electron distribution function formation in regions of diffuse aurora. *Journal of Geophysical Research: Space Physics*, *122*(4), 4251–4265. https://doi.org/10.1002/2017JA023956

Khazanov, G. V., Sibeck, D. G., & Zesta, E. (2019). The formation of electron heat flux over the sunlit quiet polar cap ionosphere. *Geophysical Research Letters*, *46*(17–18), 10201–10208. https://doi.org/10.1029/2019GL084522

Khazanov, G. V., Tripathi, A. K., Sibeck, D., Himwich, E., Glocer, A., & Singhal, R. P. (2015). Electron distribution function formation in regions of diffuse aurora. *Journal of Geophysical Research: Space Physics*, *120*(11), 9891–9915. https://doi.org/10.1002/2015JA021728

Kofman, W., & Wickwar, V. B. (1984). Very high electron temperatures in the daytime *F* region at Sondrestrom. *Geophysical Research Letters*, *11*(9), 919–922. https://doi.org/10.1029/GL011i009p00919

Kozyra, J. U., Shelley, E. G., Comfort, R. H., Brace, L. H., Cravens, T. E., & Nagy, A. F. (1987). The role of ring current O^+ in the formation of stable auroral red arcs. *Journal of Geophysical Research*, *92*(A7), 7487. https://doi.org/10.1029/JA092iA07p07487

Lemon, C., Toffoletto, F., Hesse, M., & Birn, J. (2003). Computing magnetospheric force equilibria. *Journal of Geophysical Research*, *108*(A6), 1237. https://doi.org/10.1029/2002JA009702

Lemon, C., Wolf, R. A., Hill, T. W., Sazykin, S., Spiro, R. W., Toffoletto, F. R., et al. (2004). Magnetic storm ring current injection modeled with the Rice Convection Model and a self-consistent magnetic field. *Geophysical Research Letters*, *31*(21), L21801. https://doi.org/10.1029/2004GL020914

Lyons, L. R., Gallardo-Lacourt, B., Zou, S., Weygand, J. M., Nishimura, Y., Li, W., et al. (2016). The 17 March 2013 storm: Synergy of observations related to electric field modes and their ionospheric and magnetospheric Effects. *Journal of Geophysical Research: Space Physics*, *121*(11), 10880–10897. https://doi.org/10.1002/2016JA023237

Meng, C.-I., Mauk, B., & McIlwain, C. E. (1979). Electron precipitation of evening diffuse aurora and its conjugate electron fluxes near the magnetospheric equator. *Journal of Geophysical Research*, *84*(A6), 2545–2558. https://doi.org/10.1029/JA084iA06p02545

Mishin, E. (2013). Interaction of substorm injections with the subauroral geospace: 1. Multispacecraft observations of SAID. *Journal of Geophysical Research: Space Physics*, *118*(9), 5782–5796. https://doi.org/10.1002/jgra.50548

Mishin, E., & Burke, W. (2005). Storm time coupling of the ring current, plasmasphere, and topside ionosphere: Electromagnetic and plasma disturbances. *Journal of Geophysical Research*, *110*(A7). A07209. https://doi.org/10.1029/2005JA011021

Orlova, K., & Shprits, Y. (2014). Model of lifetimes of the outer radiation belt electrons in a realistic magnetic field using realistic chorus wave parameters: Electron lifetimes in non-dipole field. *Journal of Geophysical Research: Space Physics*, *119*(2), 770–780. https://doi.org/10.1002/2013JA019596

Orlova, K., Spasojevic, M., & Shprits, Y. (2014). Activity-dependent global model of electron loss inside the plasmasphere. *Geophysical Research Letters*, *41*(11), 3744–3751. https://doi.org/10.1002/2014GL060100

Picone, J. M., Hedin, A. E., Drob, D. P., & Aikin, A. C. (2002). NRLMSISE-00 empirical model of the atmosphere: Statistical comparisons and scientific issues. *Journal of Geophysical Research: Space Physics*, *107*(A12), SIA15-1–SIA15-16. https://doi.org/10.1029/2002JA009430

Rich, F. J., & Hairston, M. (1994). Large-scale convection patterns observed by DMSP. *Journal of Geophysical Research*, *99*(A3), 3827–3824. https://doi.org/10.1029/93JA03296

Richmond, A. D., Ridley, E. C., & Roble, R. G. (1992). A thermosphere/ionosphere general circulation model with coupled electrodynamics. *Geophysical Research Letters*, *19*(6), 601–604. https://doi.org/10.1029/92gl00401

Ridley, A. J., Deng, Y., & Toth, G. (2006). The global ionosphere-thermosphere model. *Journal of Atmospheric and Solar-Terrestrial Physics*, *68*(8), 839–864. https://doi.org/10.1016/j.jastp.2006.01.008

Robinson, R. M., Vondrak, R. R., Miller, K., Dabbs, T., & Hardy, D. (1987). On calculating ionospheric conductances from the flux and energy of precipitating electrons. *Journal of Geophysical Research*, *92*(A3), 2565–2569. https://doi.org/10.1029/JA092iA03p02565

Samara, M., Michell, R. G., & Khazanov, G. V. (2017). First optical observations of interhemispheric electron reflections within pulsating aurora. *Geophysical Research Letters*, *44*(6), 2618–2623. https://doi.org/10.1002/2017GL072794

Schumaker, T. L., Carovillano, R. L., Gussenhoven, M. S., & Hardy, D. A. (1989). The relationship between diffuse auroral and plasma sheet electron distributions near local midnight. *Journal of Geophysical Research*, *94*(A8), 10061–10078. https://doi.org/10.1029/JA094iA08p10061

Schunk, R. W., & Nagy, A. F. (2009). *Ionospheres: Physics, plasma physics, and chemistry*. Cambridge University Press.

Schunk, R. W., Sojka, J. J., & Bowline, M. D. (1986). Theoretical study of the electron temperature in the high-latitude ionosphere for solar maximum and winter conditions. *Journal of Geophysical Research*, *91*(A11), 12041–12054. https://doi.org/10.1029/JA091iA11p12041

Sergeev, V. A., Sazhina, E. M., Tsyganenko, N. A., Lundblad, J. Å., & Søraas, F. (1983). Pitch-angle scattering of energetic protons in the magnetotail current sheet as the dominant source of their isotropic precipitation into the nightside ionosphere. *Planetary and Space Science*, *31*(10), 1147–1155. https://doi.org/10.1016/0032-0633(83)90103-4

Shprits, Y. Y., Li, W., & Thorne, R. M. (2006). Controlling effect of the pitch angle scattering rates near the edge of the loss cone on electron lifetimes. *Journal of Geophysical Research: Space Physics*, *111*(A12), A12206. https://doi.org/10.1029/2006JA011758

Solomon, S., Hays, P., & Abreu, V. (1988). The auroral 6,300 Å emission: Observations and modeling. *Journal of Geophysical Research*, *93*(A9), 9867–9882. https://doi.org/10.1029/JA093iA09p09867

Strickland, D. J., Book, D. L., Coffey, T. P., & Fedder, J. A. (1976). Transport equation techniques for the deposition of auroral electrons. *Journal of Geophysical Research*, *81*(16), 2755–2764. https://doi.org/10.1029/ja081i016p02755

Strickland, D. J., Daniell, R. E., Jasperse, J. R., & Basu, B. (1993). Transport-theoretic model for the electron-proton-hydrogen atom aurora: 2. Model results. *Journal of Geophysical Research*, *98*(A12), 21533–21548. https://doi.org/10.1029/93JA01645

Toffoletto, F., Sazykin, S., Spiro, R., & Wolf, R. (2003). Inner magnetospheric modeling with the Rice Convection Model. *Space Science Reviews*, *107*(1/2), 175–196. https://doi.org/10.1023/A:1025532008047

Tsyganenko, N. A., & Mukai, T. (2003). Tail plasma sheet models derived from Geotail particle data. *Journal of Geophysical Research: Space Physics*, *108*(A3), 1136. https://doi.org/10.1029/2002JA009707

Tsyganenko, N. A., Singer, H., & Kasper, J. (2003). Storm-time distortion of the inner magnetosphere: How severe can it get? *Journal of Geophysical Research*, *108*(A5), 1209. https://doi.org/10.1029/2002JA009808

Weimer, D. R. (2001). Maps of ionospheric field-aligned currents as a function of the interplanetary magnetic field derived from Dynamics Explorer 2 data. *Journal of Geophysical Research: Space Physics*, *106*(A7), 12889–12902. https://doi.org/10.1029/2000JA000295

Wing, S., Khazanov, G. V., Sibeck, D. G., & Zesta, E. (2019). Low energy precipitating electrons in the diffuse aurorae. *Geophysical Research Letters*, *46*(7), 3582–3589. https://doi.org/10.1029/2019GL082383

Wolf, R. A. (1983). The quasi-static (slow-flow) region of the magnetosphere. In R. L. Carovillano, & J. M. Forbes (Eds.), *Solar-terrestrial physics. Astrophysics and space science library* (Vol. 104). Springer. https://doi.org/10.1007/978-94-009-7194-3_14

Yang, J., Toffoletto, F. R., Wolf, R. A., & Sazykin, S. (2011). RCM-E simulation of ion acceleration during an idealized plasma sheet bubble injection. *Journal of Geophysical Research*, *116*(A5), A05207. https://doi.org/10.1029/2010JA016346

Yang, J., Toffoletto, F. R., Wolf, R. A., & Sazykin, S. (2015). On the contribution of plasma sheet bubbles to the storm time ring current. *Journal of Geophysical Research: Space Physics*, *120*(9), 7416–7432. https://doi.org/10.1002/2015JA021398